Draft version September 10, 2026
Typeset using LATEX twocolumn style in AASTeX7.0.1

A Spectral Framework for Testing the Quasi-Star Hypothesis in Little Red Dots I: Weighing LRDs by Their Super-Eddington Luminosity Ratios—No Signs of Overmassive Black Holes

Olivia Curtis,[1,2,3] Nikko J. Cleri,[1,4,2] Jakob M. Helton,[1] Joel Leja,[1,4,2] and Jason T. Wright[1,5,3]

[1]Department of Astronomy and Astrophysics, The Pennsylvania State University, 251 Pollock Road, University Park, PA 16802, USA
[2]Institute for Gravitation and the Cosmos, The Pennsylvania State University, University Park, PA 16802, USA
[3]Penn State Extraterrestrial Intelligence Center, 525 Davey Laboratory, 251 Pollock Road, Penn State, University Park, PA, 16802, USA
[4]Institute for Computational and Data Sciences, The Pennsylvania State University, University Park, PA 16802, USA
[5]Center for Exoplanets and Habitable Worlds, 525 Davey Laboratory, 251 Pollock Road, Penn State, University Park, PA, 16802, USA

ABSTRACT

We present a spectral test of the quasi-star hypothesis for Little Red Dots (LRDs) whereby a black hole grows inside a stellar-like envelope. We use `Prospector` to fit host galaxies and `TLUSTY` photospheres to four LRDs that show strong molecular or atomic absorption. We approximate each object's electron-scattered Eddington luminosity ratio, $\phi \equiv \kappa_{\rm es}\sigma T_{\rm eff}^4/(gc)$, and we use `MESA-QUEST` to simulate their envelopes. All four are super-Eddington at $\phi = 4.0$–299, although the largest value sits at the edge of our atmosphere grid and beyond our simulations. We derive envelope masses between 700–27,000 $M_\odot$, where quasi-star theory requires the black hole to be less than a third of that. GN-28074 falls five decades below its published virial mass estimate, alleviating the overmassive black hole problem. Their black holes double in mass every ~ 0.05–3.5 Myr and can produce intermediate-mass black holes in $\lesssim 30$ Myr. The two fitted components of the water-absorbing object WIDE-EGS-2974 share a single ϕ, consistent with our hypothesis that the absorption originates in an extended atmosphere. We then extend our measurements to 82 archival LRDs, finding super-Eddington photospheres throughout the population that launch winds at 1–3× their own escape speeds, which implies that LRDs evolve from being massive, continuum-driven sources to more eruptive winds as they mature and shed their outer envelopes. We thus constrain the Eddington ratios and masses of LRDs, and, for the first time, show self-consistently that quasi-stars may be the central engines powering LRDs.

Keywords: Active galactic nuclei (16) — Supermassive black holes (1663) — Black hole physics (159) — Stellar atmospheres (1584) — High-redshift galaxies (734)

1. INTRODUCTION

The discovery of "Little Red Dots" (LRDs, e.g., J. Matthee et al. 2024; J. E. Greene et al. 2024; A. de Graaff et al. 2025a; R. E. Hviding et al. 2025) stands among the most definitive achievements of the James Webb Space Telescope (JWST). The population was identified within the first year of operations (D. D. Kocevski et al. 2023; I. Labbe et al. 2025) and has since been assembled into large photometric and spectroscopic samples (V. Kokorev et al. 2024; D. D. Kocevski et al. 2025; A. Weibel et al. 2026). Even so, all aspects of their nature, namely their broad emission lines and breaks, their v-shaped UV-optical spectrum, and their lack of X-ray emission, remain challenging for any single model to describe. Most proposed explanations describe some form of black hole star (R. P. Naidu et al. 2026a; A. de Graaff et al. 2025a), a black hole enshrouded in gas that exhibits the classical features of a black hole (e.g., broad lines), together with those of a star (e.g., a Balmer break). Edge cases also compound the problem of producing a unified theory by disrupting each selection criterion as it emerges. Among them are the X-ray detections of a minority of otherwise X-ray-quiet sources (e.g., S. Fu et al. 2026; R. E. Hviding et al. 2026), the emerging long-baseline variability of individual objects (M. Cantiello et al. 2026; Z. Zhang et al. 2025), and the strong absorption features that we study here.

If a unified theory for LRDs exists, then it must account for each of these edge cases, and several of these proposed models are not mutually exclusive. Many build on the observation that an optically thick blackbody reminiscent of a stellar photosphere fits LRD optical to near-infrared continua well (A. de Graaff et al. 2025a; W. Q. Sun et al. 2026; H. Umeda et al. 2026). At surface gravities $\log g < 0$, M. C. Begelman & J. Dexter (2026), F. Gentile et al. (2026), and H. Liu et al.

Email: ocurtis@psu.edu

(2026) showed that such photospheres naturally reproduce several LRD observables, including their temperatures (A. de Graaff et al. 2025a), red colors (D. Kido et al. 2025), strong Balmer lines (X. Ji et al. 2025; A. J. Taylor et al. 2025), broad electron-scattered Balmer lines (V. Rusakov et al. 2026; J. Matthee et al. 2026), and Balmer absorption (J. Matthee et al. 2024; H. Yanagisawa et al. 2026; I. Juodžbalis et al. 2026).

The direct-collapse black hole literature, which in our usage refers to scenarios whereby a massive seed forms when a metal-poor gas cloud collapses to form a supermassive star and later a massive black hole seed without fragmenting into ordinary stars, provides several scenarios that produce optically thick photospheres around accreting seed black holes (e.g., M. C. Begelman et al. 2006; E. Pezzulli et al. 2016; Y. Luo et al. 2020; J. Roman-Garza et al. 2026). The most promising, in part because of its 1–20 Myr lifetime (A. D. Santarelli et al. 2026a; W. H. Ball et al. 2012), is the quasi-star, which forms when a gas reservoir of 10^4–$10^6\ M_\odot$, assembled through the direct collapse of an atomic-cooling halo or a dense pregalactic filament, collapses into a supermassive star whose core exhausts its support and forms a stellar-mass black hole while the surrounding envelope remains bound as a stellar envelope (M. C. Begelman et al. 2006, 2008). But supermassive stars can also be formed in runaway stellar collisions in dense star clusters (e.g., S. F. Portegies Zwart & S. L. W. McMillan 2002; M. S. Fujii et al. 2024; F. Pacucci et al. 2025; A. Rantala 2026), or in already enriched gas (S. Chon & K. Omukai 2020) that is being externally heated through Lyman-Werner radiation (V. Bromm & A. Loeb 2003; J. A. Regan et al. 2016).

In this manuscript, we do not concern ourselves with how the supermassive star forms and instead focus on what happens to the star and its environment after the core of the supermassive star collapses and leaves behind a black hole embedded in a radiation-supported, fully convective envelope. Because the envelope reprocesses the accretion luminosity, its luminosity is governed by the Eddington limit of the entire object such that the black hole is able to grow by three to four orders of magnitude within a few Myr while the photosphere resembles a cool, extremely low-gravity supergiant (W. H. Ball et al. 2011; E. R. Coughlin & M. C. Begelman 2024; J. B. Hassan et al. 2026). The inner-most regions of these objects, the so-called saturated convection layers of E. R. Coughlin & M. C. Begelman (2024), have analytic solutions that limit the black hole mass and provide a transport mechanism that moves the energy generated by accretion into the outer envelope. The saturated convection layer thus acts as the "core" of the quasi-star, acting as the energy transport layer that supports the layers above it (see Figure 1).

Now, the broader term black hole star (e.g., R. P. Naidu et al. 2026a; A. de Graaff et al. 2025a; W. Q. Sun et al. 2026) is agnostic to the formation channel and applies to any black hole surrounded by a dense gas envelope, photosphere, or atmosphere. A quasi-star is not the only path to surrounding a black hole with a dense gaseous envelope; for instance, failed winds from super-Eddington accretion flows (H. Liu et al. 2025; E. Lambrides et al. 2026; J.-R. Liu et al. 2026) or a supermassive star that collapses directly to a $\sim 10^4\ M_\odot$ black hole (D. Nandal et al. 2026) also produce black-hole-star-like spectra. In this paper, we place a quasi-star inside an extended gaseous atmosphere to explain the molecular and atomic absorption features that some sources exhibit, and throughout this manuscript, we refer to our model as a quasi-star to differentiate it from other black hole star models.

The `MESA-QUEST` framework (C. B. Campbell et al. 2025; A. D. Santarelli et al. 2026a,b) places the saturated convection layer and its outer layers into the stellar evolution code `MESA` (e.g., B. Paxton et al. 2011, 2013, 2015, 2018, 2019; A. S. Jermyn et al. 2023), where it reproduces the analytic mass ceilings and predicts photospheric temperatures near 5000 K and lifetimes of 1–20 Myr that match the LRD lifetimes that duty-cycle arguments derive (W. Q. Sun et al. 2026). J. B. Hassan et al. (2026) implement the same saturated-convection interior and set the injected luminosity to the Eddington luminosity of the whole quasi-star. They evaluate it with the local Rosseland mean opacity at the base of the inefficiently convecting layer rather than with the electron-scattering value, so their limits on how massive the black hole can grow to evolve as the star does. Their envelopes remain stable until $M_{\rm BH}/M_{\rm rad} \approx 0.33$, after which the quasi-star destabilizes and becomes a typical active galactic nucleus. Throughout, we use $M_{\rm BH}$ to denote the mass of the black hole, $M_{\rm rad}$ is the mass interior to our simulated radiative layers (see Figure 1), and $M_\bigstar$ is the mass of everything beneath the extended atmosphere (i.e., what we actually observe). We also use M_* to indicate the total stellar mass of the host galaxy.

Although models seem to indicate that such systems can remain stable for $\sim$ 1–20 Myr, A. D. Santarelli et al. (2026a) and J. B. Hassan et al. (2026) have argued that continuous accretion from the birth cloud onto the stellar envelope can counteract wind losses, thus extending the lifetime of the quasi-star, and, indeed, J. Roman-Garza et al. (2026) evolve such accreting quasi-stars to lifetimes that can reach 10–100 Myr. We note that the observed abundance of LRDs sets that timescale independently; W. Q. Sun et al. (2026) measure a duty cycle near 1% from the population's number density of $\approx 10^{-5}$ cMpc^{-3}, which they conclude to mean that every supermassive black hole may have spent $\sim$ 10 Myr in an LRD phase. M. C. Begelman & J. Dexter (2026) further interpret LRDs as the late stage of this evolution, and M. Cantiello et al. (2026) show that these cool envelopes can even cross a fundamental-mode instability strip that may explain the emerging variability of the population (Z. Zhang et al. 2025). Lastly, F. Gentile et al. (2026) have fit blackbody quasi-star models to 86 LRD spectra and reproduce the continuum shapes, Balmer breaks, and hydrogen-line luminosities of the population.

Recently, R. P. Naidu et al. (2026b) argued that LRD continua, Balmer profiles, and molecular features closely resemble the wind photospheres of η Carinae's Great Eruption and Type IIn supernovae. From the Eddington limit, the blueshifted Balmer absorption whose blue edges they measure at 240–1130 $\mathrm{km\,s^{-1}}$, the absence of rapid variability, and the low fitted gravities, they bound the black hole masses below $10^{5.1}\,M_\odot$ and conclude that their sources are super-Eddington with electron-scattering Eddington luminosity ratios $\Gamma_{\mathrm{es}} \approx 20$–50. In their picture, similar to the quasi-star case (e.g., M. C. Begelman & J. Dexter 2026), the broad Balmer lines form from electron-scattering within the low surface-gravity winds such that their widths contain no virial information.

Theoretical work on quasi-stars has meanwhile concentrated on their interiors and on how accretion onto the black hole proceeds, but much like the case for stars, only their (pseudo-)photospheres are directly observable, and it is the photosphere on which the observational literature surrounding LRDs has now converged. Blackbody continua fit the population's optical colors and shape (A. de Graaff et al. 2025a; F. Gentile et al. 2026), photospheric Balmer absorption features are seemingly ubiquitous across LRDs (J. Matthee et al. 2024; H. Yanagisawa et al. 2026; I. Juodžbalis et al. 2026), and cool, low-gravity stellar atmospheres reproduce the strongest absorption features (X. Lin et al. 2026a; H. Liu et al. 2026; B. Wang et al. 2026). We extend that and ask, if LRDs or quasi-stars have photospheres, then are there other components of stellar atmospheres that describe the upper atmospheres of these objects? Below, we describe several such structures that can reproduce the observed features of LRDs while remaining consistent with the energy budget of a quasi-star, and much of this manuscript is thus dedicated to linking these two regimes. For instance, we describe a tiered atmosphere of inflowing and outflowing material that produces Balmer progressions that are similar to the types seen in T Tauri stars (M. F. Walker 1972) or the equatorial inflow–polar-outflow geometry that J. Matthee et al. (2026) propose; we place a chromosphere above that layer, which can supply enough ionizing photons to produce the saturated He I λ10830 troughs that the data already show (e.g., The Rosetta Stone, I. Juodžbalis et al. 2024; GLIMPSE-17775, V. Kokorev et al. 2026; MoM-BH*-1, R. P. Naidu et al. 2026a; RUBIES-BLAGN-1, B. Wang et al. 2025), and we discuss how even modest magnetic fields in the photosphere and corona can confine starspots and the occasional hard narrow line that the chromosphere cannot.

In this manuscript, we derive super-Eddington luminosity ratios, and thus envelope masses, on an object-by-object basis, and, in doing so, provide a framework that can test the quasi-star hypothesis as an explanation for the central engines of LRDs. We introduce a mass-independent Eddington ratio, ϕ, constructed purely from fitted photospheric parameters, and we measure it for the four LRDs that show the strongest molecular and atomic absorption features as well as for 82 other archival sources. We thereby provide an object-by-object demonstration that $\Gamma_{\mathrm{es}} > 1$ for most LRDs. The masses that we derive follow from the fitted photosphere and luminosity alone, where the quasi-star framework supplies the simulations and closed-form solutions against which we ground every result. That is, we use the ϕ values that we derive to infer accretion factors, wind properties, magnetic starspot alternatives, and total masses, and we decompose the emission lines to separate the host's narrow system from the quasi-star's broad one, whose helium lines reveal a chromosphere and a wind of metastable helium above the photosphere. For the first time, we provide a single, falsifiable model that can test the eruptive outflow model of R. P. Naidu et al. (2026b) or the harder-than-stellar-photosphere ionization problem outlined by V. Sok et al. (2026), and we show that our model is fully consistent with the energy budget provided by quasi-stars and their saturated convection layers (E. R. Coughlin & M. C. Begelman 2024; J. B. Hassan et al. 2026; A. D. Santarelli et al. 2026a; M. C. Begelman & J. Dexter 2026).

Section 2 presents the data and our spectral fitting code. In Section 3, we develop the quasi-star model and the ϕ framework that maps it onto observations. Section 4 then reports the photospheric fits and the mass scale that follows from them. Section 5 then compares masses and mass loss rates across our fitted sample, and we also hypothesize on an evolutionary sequence for LRDs based on our results. We summarize our conclusions in Section 6, and we describe the interiors of simulated quasi-stars as well as higher-order corrections to our mass measurements in the appendices. Throughout, we assume a flat ΛCDM cosmology with $H_0 = 69.3\ \mathrm{km\,s^{-1}\,Mpc^{-1}}$ and $\Omega_{\mathrm{m}} = 0.287$ (G. Hinshaw et al. 2013).

2. OBSERVATIONS AND ATMOSPHERE MODELS

2.1. *Observations*

Our primary analysis uses a sample of 4 LRDs that show very strong molecular and atomic absorption features, as well as an archival sample of 82 LRDs, most of which have broad Balmer features. Our main sample of 4 galaxies is comprised of J1025+1402 (redshift $z = 0.1007$, hereafter "The Egg," X. Lin et al. 2026a) which shows a very strong Ca II triplet, GN-28074 ($z = 2.26$, "The Rosetta Stone," I. Juodžbalis et al. 2024) which shows a tentative detection of a Ca II triplet, and WIDE-EGS-2974 ($z = 2.3203$) and UNCOVER-A2744-20698 ($z = 2.42$; B. Wang et al. 2026) both of which are two LRDs that show strong molecular water absorption. Going forward, we collectively term these two "water dots" after the molecular water band that distinguishes them.

We use JWST NIRSpec PRISM observations of both water dots, taking the reduced 1D spectra of B. Wang et al. (2026) from the DAWN JWST Archive (K. E. Heintz et al. 2025; A. de Graaff et al. 2025b). WIDE-EGS-2974 lies in the Extended Groth Strip and comes from the NIRSpec WIDE GTO Survey (GTO 1213, PI P. Ferruit; M. V. Maseda et al. 2024). UNCOVER-A2744-20698 sits behind the Abell 2744 cluster field and comes from the Ultradeep NIRSpec and NIRCam ObserVations before the Epoch of Reionization survey (UNCOVER; GO 2561, PIs I. Labbé and R. Bezanson; R. Bezanson et al. 2024). Both sources show strong molecular water absorption in the 12,800–14,500 Å band.

The Egg is a local LRD from the Sloan Digital Sky Survey (D. G. York et al. 2000). X. Lin et al. (2026a) identified it as a low-redshift analog of the high-z LRD population and observed it with LBT MODS (3300–10,000 Å, $R \sim 800$–1700) and Magellan FIRE (0.8–2.5 μm). The Egg shows very high equivalent width (EW) metal absorption, including the Ca II triplet (16.7 ± 0.5 Å), along with weaker low-ionization metal features characteristic of cool stellar photospheres (X. Lin et al. 2026a). H. Liu et al. (2026) fit these observations with a suite of low surface gravity ($\log g < 0$) TLUSTY (I. Hubeny 1988; I. Hubeny et al. 2021) atmosphere models and found that The Egg requires an effective temperature $T_{\rm eff} = 4500$ K and surface gravity $\log g = -2.90$ to explain its strong absorption features (§ 2.2).

The Rosetta Stone (I. Juodžbalis et al. 2024) lies in the Great Observatories Origins Deep Survey North (GOODS-N) field and comes from the JWST Advanced Deep Extragalactic Survey (JADES; GTO 1181, PIs D. Eisenstein and P. Ferruit; D. J. Eisenstein et al. 2026). We use its JWST NIRSpec observations in PRISM mode and in three medium-resolution gratings (G140M/F070LP, G235M/F170LP, and G395M/F290LP, all at $R \sim 1000$). Its continuum displays the characteristic v-shape and red optical colors, and it has a virial estimate of $\log(M_{\rm BH}/M_\odot) \approx 8.5$ (I. Juodžbalis et al. 2024). Much like The Egg, The Rosetta Stone shows signs of a Ca II triplet.

Our broader sample consists of 82 supplementary LRDs, which we draw from four archival catalogs and five individually published sources. We select these sources for our wind analysis that we perform in Section 5.2, where we assemble a large population of sources that have a published Balmer absorption to test different mass-loss schemes and how they vary as a function of our fitted super-Eddington accretion rate. The absorption-velocity sample of R. P. Naidu et al. (2026b) contributes 11, the Red Unknowns: Bright Infrared Extragalactic Survey (RUBIES) contributes thirty through R. E. Hviding et al. (2025) and eight through V. Sok et al. (2026), and the low-redshift DESI sample contributes 28 (e.g., K. Park et al. 2026; X. Lin et al. 2026b). The remaining five are A2744-QSO1 (X. Ji et al. 2025; F. D'Eugenio et al. 2026), GLIMPSE-17775 (V. Kokorev et al. 2026), MoM-BH*-1 (R. P. Naidu et al. 2026a), and the grating-detected CEERS-6126 and UDS-31092 of D. D. Kocevski et al. (2025). We restrict the low-redshift DESI sources to the spectroscopically vetted (LRDs)[2] sample (X. Lin et al. 2026b). We take the JWST spectra from the DAWN JWST Archive and the DESI spectra from Data Release 1 (DESI Collaboration et al. 2026), and we fit each at its native resolution with the framework of Section 2.3.

2.2. *TLUSTY Atmospheres*

We model the photospheric emission with the synthetic spectral library of H. Liu et al. (2026), which is computed with the plane-parallel radiative-transfer code TLUSTY (I. Hubeny 1988; I. Hubeny et al. 2021). Conventional stellar atmosphere grids terminate near $\log g \approx 0$, whereas LRD continua demand gravities several dex lower, so H. Liu et al. (2026) extended the calculations into the radiation-pressure-dominated regime where the atmosphere approaches the local Eddington limit. Each model solves the coupled radiative transfer and hydrostatic structure under LTE for a scaled solar composition and returns the emergent spectrum together with the photospheric density, which falls with gravity and controls the strengths of the pressure-sensitive features that anchor our fits (e.g., the Ca II triplet and the molecular bands of H_2O, TiO, and MgH; X. Lin et al. 2026a; H. Liu et al. 2026).

The library contains 233 models that span $T_{\rm eff} = 2000$–7500 K, $\log g = -4$ to $+1.5$, metallicities [M/H] $= -2$, -1, and 0, and it includes microturbulent velocities of 2 and 10 km s^{-1}. Below 4000 K, the library covers only [M/H] $= -1$, so we fix the photospheric metallicity there for objects that are cooler than that. Between the nodes, we bracket the sampled temperatures and gravities by the two nearest grid values and interpolate linearly between the two nodes. The models are hydrostatic and plane parallel, so our fitted gravities inherit the extended-atmosphere and outflow biases that we quantify below.

2.2.1. *Consequences of Modeling in Hydrostatic Equilibrium*

An important caveat is that the atmospheric models assume the atmosphere is plane-parallel and in hydrostatic equilibrium (see, e.g., T. Lebzelter et al. 2012; I. Hubeny et al. 2021; G. González-Torà et al. 2023; H. Liu et al. 2026). H. Liu et al. (2026) directly quantify the assumption of hydrostatic equilibrium while creating their models, and we adopt their formalism since our ϕ values depend on it (Section 3.3). A spectrum does not measure the local acceleration due to gravity, g, directly. It instead responds to the pressure and temperature stratification of the layers that form it, since those two set the ionization balance, the electron pressure, and the opacities. A closure relation is then needed to convert that pressure into a gravity. Hydrostatic equilibrium can provide that closure, but that does not hold at an outflow layer that is accelerating. H. Liu et al. (2026) retain the dynamical term in the radial equation of motion, so the parameter that their library constrains is the net effective gravity $g_{\rm net} \equiv g - g_{\rm dyn}$. Here, $g = GM_{\rm tot}/R^2$ is the true local gravity for a gravitational constant G, a mass $M_{\rm tot}$ that is enclosed by the photosphere, and a photospheric radius R, while $g_{\rm dyn} \simeq -{\rm sgn}(dv^2/dR)\, v^2/R$ is a catchall for any inward or outward motion of that layer at a radial velocity v, where sgn refers to the signum function. Their photospheric density is $\rho_{\rm ph} \approx 2\mu m_p (g_{\rm net} - g_{\rm rad})/(3k_B T_{\rm eff} \kappa_{\rm ph})$, where μ is the mean molecular weight, m_p is the proton mass, k_B is the Boltzmann constant, and $\kappa_{\rm ph}$ is the photospheric opacity. The radiative acceleration, $g_{\rm rad} = \kappa_F \sigma T_{\rm eff}^4/c$, follows from the flux-mean opacity κ_F, the Stefan–Boltzmann constant σ, and the speed of light c. A fit therefore constrains the difference $g - g_{\rm dyn}$, though independent constraints on the gas motion can separate the two terms. H. Liu et al. (2026) note that their library therefore applies to any geometry whose energy source sits deep inside an optically thick atmosphere, so we measure $g_{\rm net}$ whether or not the photosphere we fit is a static surface.

H. Liu et al. (2026) then treat the atmospheres that approach the Eddington limit in two ways that affect how we can interpret our $\log g$ measurements. In the first case, the inferred gravity is moderately low, so the outer layers stay sub-Eddington and hydrostatic while the inner layers pass the local Eddington limit. H. Liu et al. (2026) hold the gas pressure at its maximum value through those inner layers since a gas-pressure inversion is unstable and the inner atmosphere can smear it out (Y.-F. Jiang et al. 2015), and they show that the modification leaves the synthetic spectra largely unchanged since the outer layers, where most spectral features form, end up remaining in hydrostatic equilibrium. In the second case, the gravity is low enough that the whole atmosphere passes the Eddington limit, so H. Liu et al. (2026) then remove the radiative acceleration from the hydrostatic equation and describe the result as an optically thick gas layer rather than as an atmosphere, and they expect such a layer to be spatially extended with a high radial velocity. In Appendix A, we show that the internal structure of our quasi-star simulations more closely aligns with the first case.

Lastly, their convention for $g_{\rm dyn}$ also biases our fits away from the eruptive super-Eddington envelopes that we derive below. Gas that escapes the system has $dv^2/dR > 0$ and gives $g_{\rm net} > g$, so the photosphere is actually accelerating outward. Rotation, turbulence, and infall keep the gas bound and give $g_{\rm net} < g$, and we treat those corrections in Appendix B.

2.3. *Spectral Modeling*

We fit every source with a single forward model that we build with `Prospector` (B. D. Johnson et al. 2021).[6] Our model sums one (or two in the case the target has a cold component; B. Wang et al. 2026) TLUSTY photospheres with a host galaxy that `FSPS` (C. Conroy et al. 2009) generated under a six-bin continuity star-formation history using a P. Kroupa (2001) initial mass function and a free stellar metallicity parameter. We then also add B. T. Draine & A. Li (2007) dust emission with its minimum radiation-field intensity $U_{\rm min}$, polycyclic aromatic hydrocarbon mass fraction $q_{\rm PAH}$, and high-intensity fraction γ left free, and we attenuate every component with a shared foreground dust screen. Each `TLUSTY` photosphere has its own temperature, surface gravity, and luminosity terms. After performing a series of tests to find which dust laws best fit our sources, we adopt a Small Magellanic Cloud attenuation law (K. D. Gordon et al. 2003) for every source in this work, following X. Lin et al. (2026a) for The Egg and the local sample. All sampling is performed with dynamic nested sampling (`dynesty`; J. S. Speagle 2020), which also returns the Bayesian evidence $\mathcal{Z}$, i.e., the likelihood integrated over the prior, which we use to compare model variants through their $\log_e$ evidence differences $\Delta \ln \mathcal{Z}$.

We fit every spectrum in its native pixels, where we add a systematic floor in quadrature to the pipeline uncertainties, 5% for The Egg and 10% for the JWST sources. The MODS-R arm of The Egg is measured to about one percent, so its five percent floor sets the uncertainty there, while the archival spectra sit near twenty percent and their floor adds little. Where a source has more than one spectrum, we fit each over a fixed rest-frame range so that no pixel enters the likelihood twice. We correct for one measured cross-calibration offset. Since FIRE runs 9.6 percent fainter than MODS-R in the 7550 to 8450 Å overlap the two share, we scale the FIRE fluxes and uncertainties by a fixed factor of 1.106. We leave MODS-B and MODS-R uncorrected, as they agree to one percent. We forward-model each arm at one fixed resolving power. These are $R = 1850$ and 2250 for the MODS G400L and G670L arms, $R = 6000$ for the FIRE echelle, $R = 100$ for NIRSpec PRISM, $R = 1000$ for the NIRSpec medium gratings, and $R = 2500$, 3500, and 4500 for the DESI B, R, and Z cameras. We fit UNCOVER-A2744-20698 at $R = 300$ instead, which is the PRISM spectral resolution where its water band falls, and we verify that its photospheric parameters move by less than a posterior width from the $R = 100$ run.

[6] Our `Prospector` fork, which implements the TLUSTY photosphere basis alongside the code's stock stellar population sources, is available at https://github.com/o-curtis/prospector-tlusty.

We then mask the emission lines before fitting, using a single emission line list that masks the Balmer and Paschen series, He I λ10830, He II λ4686, [O III] $\lambda\lambda$4959, 5007, [Ne III] λ3869, [O II] λ3727, Mg II λ2798, and C II] λ2326. For our 4 primary sources, we modified the list to remove only lines that were actually present in the data, but, for our 82 archival fits, this full list was used. We are justified in masking the emission lines since our photospheric models are in LTE and contain no emission features (H. Liu et al. 2026). Models in LTE are thus most accurate in the continuum and absorption features (I. Hubeny 1988; I. Hubeny et al. 2021), while a robust forward model of the emission lines would require accounting for the host narrow lines, the electron-scattered broad lines (J. E. Greene et al. 2024; R. E. Hviding et al. 2025), lines broadened in the winds, absorption (V. Rusakov et al. 2026; R. P. Naidu et al. 2026b), as well as any narrow coronal or chromosphere emission (e.g., F. Gentile et al. 2026, Paper II), which is beyond the scope of this study.

We also mask the Balmer break from our fits, which we define as the region between 3400–4100 Å. As H. Liu et al. (2026) describe, their plane-parallel assumption fails to fully model the break, especially near the Ca II H and K line cores, and they state that this assumption is likely to break down for the cold, dense, extended atmospheres like the ones that we propose in the following section. Our emission line masking already masks most of our PRISM data in this region, whereas our DESI sources resolve individual lines in the region. Independent testing has shown that, while leaving this region unmasked does not change our population-level results, the DESI sources can have their fitted $\log g$ values inflated by $\sim$ 0.6 dex if the region is left unmasked, but the unmasked PRISM fits return surface gravities consistent to within 1σ.

We fit the 53 archival PRISM sources with one uniform configuration with the parameters described above, i.e., a single `TLUSTY` photosphere plus a host galaxy. Since PRISM cannot resolve the line broadening, we do not broaden the LRD component, and we fix the microturbulence term to $2\ \mathrm{km\,s^{-1}}$ and the photospheric metallicity to $[\mathrm{M/H}] = -1$. The latter is done to ensure that our archival PRISM fits are using the exact same model as our water dots, modulo the additional cold component that we describe below. We then use a free dust screen, which leaves 14 free parameters in total. We fit GLIMPSE-17775 instead on its G395M continuum, and we fit the 28 DESI sources at each camera's resolution with the metallicity, microturbulence, and broadening left free, giving 18 free parameters there.

Since our four primary sources have unique spectral absorption features, we make minor changes to our unified model, most of which are to circumvent library limitations and to account for the fact that two of our primary sources show atmospheric absorption lines. For instance, The Egg and The Rosetta Stone need to have their Ca II triplets broadened (e.g.,

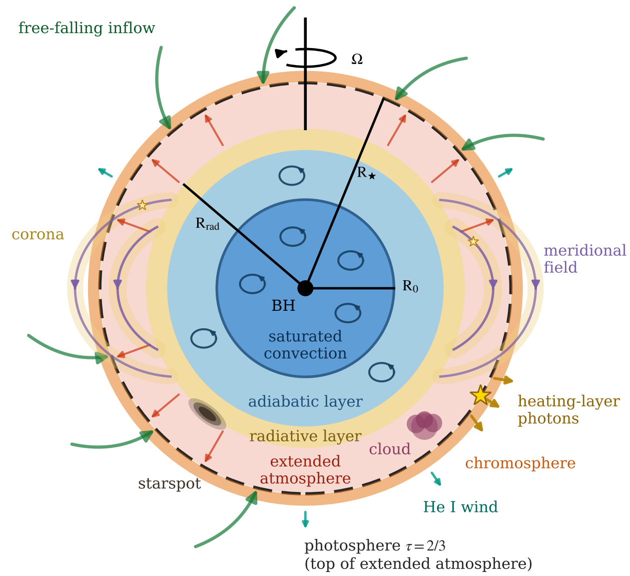

Figure 1. A cartoon of the quasi-star hypothesis, drawn in the meridional plane at a late evolutionary stage and not to scale. Each labeled structure is either an analytic part of the quasi-star model (e.g., the saturated convection layer), is solved by `MESA-QUEST` (the adiabatic, and radiative layers), is motivated by an observation in this paper (the extended atmosphere, and the inflow–outflow interface), is a plausible explanation for one of our observations (starspots and clouds), or is a feature that will be discussed in Paper II (the chromosphere, the corona, and the He I wind). A black hole sits at the center of the saturated-convection zone, which is surrounded by an adiabatic layer, a physically thin radiative layer, and an optically thick extended atmosphere. The dashed circle is the $\tau = 2/3$ photosphere near the top of that atmosphere, which is partially confined from above by free-falling inflowing material (green). The three marked radii are the inner boundary of the simulated envelope (R_0), the top of the radiative layer (R_{rad}), and the photosphere ($R_\bigstar$). A thin chromosphere (orange ring) surrounds the photosphere, and its heating-layer photons (gold star and arrows) ionize the wind above (teal arrows), where recombination can populate metastable He I. We also show magnetically confined starspots on the stellar surface, a dense cloud in the extended atmosphere, closed meridional field loops throughout the atmosphere, and a tenuous magnetically heated corona (orange haze) with magnetic reconnection sites (small stars), and Ω marks the rotation axis.

I. Juodžbalis et al. 2024; H. Liu et al. 2026) since the library atmospheres include no broadening beyond their thermal microturbulent widths (H. Liu et al. 2026). We thus fit *The Egg* across all 3 of its arms with a single photosphere, a free microturbulence parameter, a free photospheric metallicity, and an atmospheric broadening term that we confine to ∼115–135 $\mathrm{km\,s^{-1}}$ with least-squares fits to the Ca II triplet (18 free parameters). Since we have $R \gtrsim 1000$ spectra for The Egg, we leave the region around its Balmer break unmasked and instead only mask the region around the Ca H and K lines following the recommendations of H. Liu et al. (2026). Lastly, we upweight the triplet by 15× to increase the signal coming from those important features, which is necessary to prevent the continuum pixels from dominating the fit.

We fit *The Rosetta Stone* with the same configuration across its 3 medium gratings. Since the spectral resolution is much more coarse than the available data for The Egg, we fix the microturbulence term to 2 $\mathrm{km\,s^{-1}}$ (the default of the H. Liu et al. (2026) library). Similarly, since its Ca II triplet is more tenuous (I. Juodžbalis et al. 2024), sitting inside the broad Paschen and O I λ8446 emission (Section 2.1), we leave the broadening term free between 50–800 $\mathrm{km\,s^{-1}}$ (17 free parameters).

We fit both water dots with the same model that we used to fit the archival PRISM spectra, except that we also include a cold photosphere that shares the same dust screen and adds its own temperature, gravity, and luminosity (17 free parameters each). We fix the metallicity to [M/H] = −1 due to the fact that it is the only metallicity in our library that goes below 3000 K, which is approximately the photo-dissociation point of water. Lastly, we upweight the water band 5× for the same reason as the Ca II triplet above.

3. QUASI-STARS

The innermost layer of the quasi-star is its saturated convection layer. Convection saturates when it carries the largest flux that the gas can transport (i.e., roughly the pressure times the sound speed through each surface) and is thus the limit at which convection can sustain super-Eddington energy transport (M. C. Begelman 2001) and convection-dominated accretion flows (E. Quataert & A. Gruzinov 2000). Quasi-stars are thought to occur when the core of a supermassive star formed inside a rapidly inflowing gas cloud collapses, eventually forming a newborn black hole after Myr timescales. Accretion onto this black hole then puts more power into the surrounding gas than ordinary convection can carry. This drives the innermost envelope to saturation, forming a stellar envelope (e.g., M. C. Begelman et al. 2006, 2008; M. C. Begelman 2010; W. H. Ball et al. 2011, 2012; E. R. Coughlin & M. C. Begelman 2024). Notably, the saturated convection layer has an analytical solution (E. R. Coughlin & M. C. Begelman 2024), and, more recently, the outer envelopes have been modeled with stellar evolution codes using the analytical solution of the saturated convection as an inner boundary condition (e.g., W. H. Ball et al. 2011, 2012; J. B. Hassan et al. 2026; A. D. Santarelli et al. 2026a).

Figure 1 is a cartoon of our model (not to scale). Quasi-stars can drive outflows off of the radiative layer (D. Fiacconi & E. M. Rossi 2016; A. D. Santarelli et al. 2026a), and we predict that the material this outflow lifts can form an extended atmosphere whose $\tau = 2/3$ surface is the (pseudo-)photosphere that we observe, much in the same way that stellar envelopes near the Eddington limit extend while staying hydrostatic (see, e.g., G. Gräfener et al. 2012 for an application of this to luminous blue variables and Wolf-Rayet stars). The in-falling birth-cloud material can confine that atmosphere from above (M. C. Begelman et al. 2008; M. C. Begelman 2010), where the birth cloud accreting onto the quasi-star can extend its life by adding mass to the envelope (A. D. Santarelli et al. 2026a; J. B. Hassan et al. 2026; J. Roman-Garza et al. 2026). We add to this picture several other components of stellar atmospheres, such as starspots, heating layers, clouds, field loops, and a chromosphere, each of which we discuss in the following sections or in Paper II. In brief, the saturated convection layer is determined by theory, `MESA` then models the adiabatic and radiative layers out to its own $\tau = 2/3$ surface, and we treat the wind with the mass-loss model of Section 3.2 and the extended atmosphere with the conservation laws of Section 3.4. We do not claim that every LRD has each of these components; they are instead collected into one figure to highlight the diversity of phenomena that could be affecting LRD spectra.

We note that none of the emission or absorption features in Figure 1 are formed below the photosphere since electron scattering in the atmosphere broadens the lines and the chromosphere supplies the modest ionizing power that the helium lines need (see also Paper II). Models that keep an active galactic nucleus at the center of an optically thick cocoon instead require a low-density funnel or a partially covering gap through which the central ultraviolet escapes to a broad-line region above the photosphere (J.-R. Liu et al. 2026; P. Madau & R. Maiolino 2026). A quasi-star cannot sustain that geometry since, dynamically, the outermost layers are highly convective and radiation dominated (E. R. Coughlin & M. C. Begelman 2024; J. B. Hassan et al. 2026). The optical depth of the overlying material can reach $\tau \approx 10^4$ where the free-fall time is six years at the inner boundary and 25 at the photosphere while convection drives mixing in decades, so any hole in the envelope would quickly reseal within years.

3.1. *The `MESA-QUEST` Simulations*

We evolve the model described in Section 3 with `MESA-QUEST` (C. B. Campbell et al. 2025; A. D. Santarelli et al. 2026a,b), which is a modification of the `MESA` stellar evolution code that replaces the innermost boundary of the hydrostatic envelope with conditions that describe an accreting central black hole. The code sets the coordinate of the inner mass to $m(R_0) = M_{\rm BH} + M_{\rm int}$, which includes the gas interior to the inner boundary ($M_{\rm int}$), and sets the inner luminosity to $l(R_0) = L_{\rm BH}$ at the inner boundary radius R_0. The outer boundary is the standard `MESA` photospheric condition in which a gray Eddington $T(\tau)$ relation sets the temperature at the `MESA-QUEST` model's $\tau = 2/3$ surface (i.e., the top of the radiative layer $R_{\rm rad}$), and the total surface pressure is $(2/3)(g/\kappa)(1+\Gamma_{\rm ph})$, where $\Gamma_{\rm ph}$ is the local Eddington ratio of the escaping flux. Every model is therefore always in hydrostatic equilibrium by construction. The injected luminosity is

$$L_{\rm BH} = \alpha_{\rm acc} \frac{4\pi G M_{\rm rad} c}{\kappa_0}, \tag{1}$$

c the speed of light, κ_0 the Rosseland mean opacity of the innermost zone, and $\alpha_{\rm acc}$ a dimensionless accretion factor that absorbs the uncertain physics of the central engine, including rotation, magnetic fields, and photon trapping (A. D. Santarelli et al. 2026a).[7] The corresponding BH growth rate is $\dot{M}_{\rm BH} = (1-\varepsilon)L_{\rm BH}/(\varepsilon c^2)$, with a radiative efficiency $\varepsilon = 0.1$ throughout.

Our models use `MESA` r25.12.1 with the low-temperature molecular opacities of AESOPUS (P. Marigo & B. Aringer 2009), which include the H_2O, TiO, and CO bands that dominate at our photospheric temperatures of interest. We seed the runs with supermassive stars of 10^4, 10^5, and $10^6\ M_\odot$, and distribute their metals at solar abundance ratios using the same metallicities that our `Prospector` fit returns. We do not seed below this level since a quasi-star envelope must stay radiation-pressure dominated (M. C. Begelman et al. 2008; E. R. Coughlin & M. C. Begelman 2024). Independent testing shows that this assumption breaks down at lower masses, where the ratio between the gas pressure and the total pressure rises to $\beta \sim 10\%$ for $10^3\ M_\odot$ seeds and $\beta \sim 28\%$ for $10^2\ M_\odot$ seeds, the latter of which fails to initialize entirely. Similarly, J. Roman-Garza et al. (2026) find that the general-relativistic instability that allows a supermassive star to transition into its quasi-star phase is only possible at envelope masses $\gtrsim 10^4 M_\odot$, implying that our seed masses align with what can be created by a supermassive star. We evolve our simulations until the black hole mass exceeds $M_{\rm BH}/M_{\rm rad} \approx 0.33$, above which the quasi-star solution breaks down (E. R. Coughlin & M. C. Begelman 2024; J. B. Hassan et al. 2026). That limit is due to the fact that a quasi-star radiates near the Eddington limit of the total star, so the envelope must stay massive enough to confine the outgoing radiation hydrostatically. The exact ratio depends on how the boundary condition is defined; E. R. Coughlin & M. C. Begelman (2024) analytically derive caps of $M_{\rm BH}/M_{\rm rad} \approx 0.55$–$0.62$, while the `MESA` simulations run by J. B. Hassan et al. (2026) find this instability occurs around 0.33, and we adopt the latter since we similarly evolve our quasi-stars with `MESA`.

3.2. *Mass Loss*

Quasi-stars drive outflows off of the radiative layer such that the $\tau = 2/3$ surface that we observe instead sits atop an extended atmosphere similar to those seen around asymptotic giant branch (AGB) stars (see below). We use the word wind for the transonic flow that escapes above the photosphere, following the usual meaning of the term for hot stars (H. J. G. L. M. Lamers & J. P. Cassinelli 1999), and we call the slower material beneath the photosphere the extended atmosphere, after the levitated layers of cool AGB stars (S. Höfner & H. Olofsson 2018; G. González-Torà et al. 2023). In steady state, the mass that leaves the radiative layer travels through the extended atmosphere and escapes in the wind at a single rate, $\dot{M}_{\rm wind}$.

Super-Eddington mass loss follows the `MESA-QUEST` prescription (A. D. Santarelli et al. 2026a), i.e., a power-law fit to the radiation-driven outflow solutions of D. Fiacconi & E. M. Rossi (2016),

$$\dot{M}_{\rm wind} = 1.4\times10^{-4}\left(\frac{M_\bigstar}{M_\odot}\right)^{0.96}\left(\frac{M_{\rm BH}}{M_\odot}\right)^{0.17} M_\odot\ {\rm yr}^{-1}. \tag{2}$$

Equation (2) is an upper-limit on the maximum mass loss rate that radiation pressure can drive under the assumption that there is no competing in-falling ram pressure that can hold down the outflow (D. Fiacconi & E. M. Rossi 2016; A. D. Santarelli et al. 2026a). Although this term was originally derived to describe the radiation-driven outflows coming off of the radiative layers of quasi-stars, we use it interchangeably to describe the wind coming off of the extended atmosphere since both regions are dominated by radiation. Modeling such winds as a steady, spherically symmetric flow at its terminal speed v_∞, with density $\rho(r) = \dot{M}_{\rm wind}/(4\pi r^2 v_\infty)$ thus yields

$$\dot{M}_{\rm wind} \le \frac{8\pi\, v_\infty R_\bigstar}{3\,\kappa_{\rm es}}. \tag{3}$$

3.3. *The Eddington Ratio and LRD Observables*

Spectral fitting returns the effective temperature and surface gravity of a photosphere but not its mass or radius. We therefore work with two Eddington ratios,

$$\Gamma_{\rm es} \equiv \frac{L}{L_{\rm Edd}(\kappa_{\rm es})}, \qquad \phi \equiv \frac{\kappa_{\rm es}\sigma T_{\rm eff}^4}{g_{\rm net} c}, \tag{4}$$

where L is the bolometric luminosity, $L_{\rm Edd} = 4\pi G M_\bigstar c/\kappa_{\rm es}$ is its Eddington luminosity, σ the Stefan–Boltzmann constant, and $g_{\rm net}$ is the fitted gravity of Section 2.2. That is, while $\Gamma_{\rm es}$ is a physical property of the photosphere, ϕ is what we actually observe due to the effects of $g_{\rm dyn}$ described above. The two are thus equivalent only when $g_{\rm net} \approx g$ via $L = 4\pi R^2 \sigma T_{\rm eff}^4$ and $g = GM/R^2$, which makes ϕ a spectroscopic proxy for $\Gamma_{\rm es}$. Any spectroscopic fit therefore places a source on an iso-ϕ line in the $\log g$–$T_{\rm eff}$ plane. We call the variable ϕ rather than $\Gamma_{\rm es}$ due to this approximation, and we describe below how other factors like rotation or magnetic support can shift $g_{\rm net}$ away from g.

Our `MESA-QUEST` simulations reproduce super-Eddington behavior throughout the envelope, where the local Eddington

[7] We note that A. D. Santarelli et al. 2026a use α for this term, but we use $\alpha_{\rm acc}$ to separate it from the mixing-length theory $\alpha_{\rm mlt}$.

ratio rises above unity causing density inversions to fill most of the interior (see Appendix A). A `MESA` simulation cannot follow that behavior out to the surface, however, since a hydrostatic code has no way to drive a wind (see Appendix A). What each simulation returns at its photosphere is therefore the surface that a quasi-star would have in the absence of any mass loss. `MESA-QUEST` therefore only models the adiabatic and radiative layers of Figure 1, while our fitted temperatures and gravities measure the extended atmospheres. We discuss in Section 3.4 how our ϕ definition allows us to measure how much the outflow has expanded the extended atmosphere.

3.3.1. *Mapping Observations to Simulations*

A shared premise between the analytical and numerical treatments of quasi-stars is the fact that they radiate at approximately the Eddington limit of the whole envelope (W. H. Ball et al. 2011; E. R. Coughlin & M. C. Begelman 2024; J. B. Hassan et al. 2026; A. D. Santarelli et al. 2026a). This quantity, $\alpha_{\rm acc}$ in the `MESA-QUEST` formalism, maps to our fitted ϕ through

$$\alpha_{\rm acc} = \phi\, f(Z), \qquad f(Z) \equiv \frac{\kappa_0(Z)}{\kappa_{\rm es}}, \tag{5}$$

where κ_0 is the Rosseland mean opacity of the innermost cell that is simulated by `MESA-QUEST` (i.e., the base of the adiabatic convection layer; A. D. Santarelli et al. 2026a), and $f(Z)$ is its ratio to $\kappa_{\rm es}$ that sets the metallicity dependence. A metal-free interior is hot enough that $\kappa_0 \approx \kappa_{\rm es}$ and $\phi \approx \alpha_{\rm acc}$, but metals can raise κ_0 through bound-free and free-free opacity. We calibrate f on our converged models using the value of κ_0 that we derive at time $t = 0$, finding that $f(Z) = 1.15$. However, as the simulations evolve, the opacity of the innermost cell evolves such that any observed ϕ only fixes $\alpha_{\rm acc}$ to within $\pm 20\%$, which we propagate throughout the rest of our calculations.

The value of $L_{\rm Edd}$, and with it Equation (5), depends on the opacity and on the layer at which we read it. Written as a function of radius, the local radiative component of the Eddington ratio is

$$\Gamma_{\rm rad}(r) = \frac{\kappa(r)\, \ell_{\rm rad}(r)}{4\pi G m(r) c}, \tag{6}$$

where $\kappa(r)$ is the local Rosseland mean opacity, $\ell_{\rm rad}(r)$ the luminosity carried by radiative diffusion, and $m(r)$ the enclosed mass. Quasi-star models evaluate this ratio either at the base of the radiative layer in the hot, metal-poor limit $\kappa_0 \approx \kappa_{\rm es}$ (e.g., E. R. Coughlin & M. C. Begelman 2024) or at the base of the adiabatic convection layer, where κ_0 rises to 0.5–0.75 $\rm cm^2\,g^{-1}$ as the envelope evolves (J. B. Hassan et al. 2026; A. D. Santarelli et al. 2026a).

Super-Eddington in our usage therefore means that $\phi > 1$ for the quasi-star as a whole, referenced to its total mass $M_\bigstar$. It does not imply a lack of hydrostatic equilibrium, and every source that we fit with `MESA-QUEST` is indeed modeled in equilibrium due to the nature of the code. The corresponding local radiative ratio at the top of the radiative layer is $\Gamma_{\rm ph}(R_{\rm rad}) \approx \phi\, \kappa(R_{\rm rad})/\kappa_{\rm es}$, reduced by the small photospheric Rosseland opacity $\kappa(R_{\rm rad}) \ll \kappa_{\rm es}$.

We use Equation (5) to map observations to simulations throughout. Appendix B takes this mapping a step forward, showing how this ratio behaves in hydrostatic equilibrium under the effects of rotation, magnetic-support, and inflow–outflow corrections, where we confirm that none of these assumptions change our final black hole masses by more than a factor of two. Equation (5) therefore makes ϕ a fitted quantity that depends only on the accretion factor and the metallicity, $\phi = \alpha_{\rm acc}/f(Z)$, at every mass and age. Our fitted temperatures and gravities therefore measure $\alpha_{\rm acc}$, and we can use the fitted luminosities to derive masses through Equation (11) and radii through the Stefan–Boltzmann law. In the $T_{\rm eff}$–$\log g$ plane, a quasi-star of known $\alpha_{\rm acc}$ and metallicity must sit on the iso-ϕ line

$$\log g = \log\left[\frac{\kappa_{\rm es}\, \sigma T_{\rm eff}^4\, f(Z)}{\alpha_{\rm acc}\, c}\right]. \tag{7}$$

3.4. *ϕ Conservation in an Extended Atmosphere*

Luminosity must be conserved from the top of the radiative layer to the photosphere of the extended atmosphere, at radius $R_\bigstar$, such that the Stefan–Boltzmann law and Newtonian gravity relate the effective temperature $T_{\rm eff}$ (i.e., the local flux $F = \sigma T_{\rm eff}^4$, not the gas temperature) and Newtonian gravity g at the photosphere to the temperature $T_{\rm eff,rad}$, gravity $g_{\rm rad}$, and radius $R_{\rm rad}$ of the radiative layer as

$$T_{\rm eff} = T_{\rm eff,rad}\left(\frac{R_{\rm rad}}{R_\bigstar}\right)^{1/2}, \qquad g = g_{\rm rad}\left(\frac{R_{\rm rad}}{R_\bigstar}\right)^2. \tag{8}$$

Both relations follow from the conservation of L and $M_\bigstar$ and from Newtonian gravity alone, so neither assumes hydrostatic balance. Under hydrostatic equilibrium, $g_{\rm net} \approx g$ (see Section 2.2), and substituting Equation (8) into Equation (4) shows that the factors of $R_\bigstar$ cancel exactly, providing a relation between ϕ and its corresponding value at the top of the radiative layer, $\phi_\star$, as

$$\phi = \frac{\kappa_{\rm es} L}{4\pi G M_\bigstar c} = \phi_\star. \tag{9}$$

An extended atmosphere, under the assumption that $g_{\rm net} \approx g$, thus conserves the Eddington ratio. The $\tau = 2/3$ surface then moves outward, so the photosphere that we observe is cooler and has a lower gravity than the radiative layer beneath it, much in the same way that the extended atmospheres of AGB stars are cooler than their interior radiative layer. In some

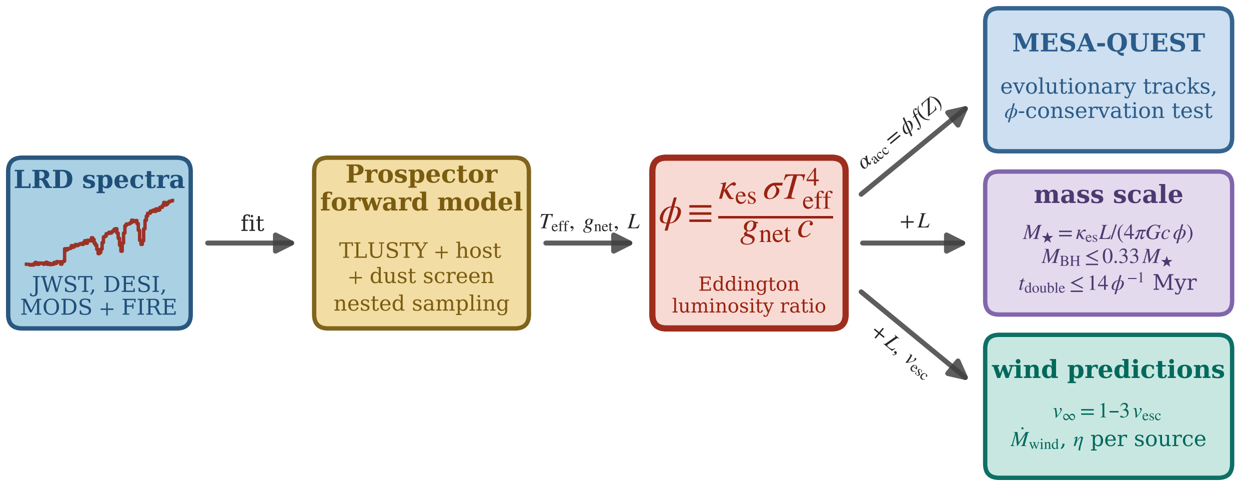

Figure 2. Flowchart of the methods presented in this manuscript. We first fit each spectrum with a `Prospector` model that includes one (or multiple) `TLUSTY` photospheres with a host galaxy, which we use to derive the Eddington luminosity ratio ϕ from the fitted effective temperatures, surface gravities, and luminosities of our quasi-stars. The rest of this manuscript uses this parameter to test various aspects of the quasi-star hypothesis. For instance, we match ϕ to the accretion factor $\alpha_{\rm acc}$, which allows us to more closely simulate each of our sources with `MESA-QUEST`. We can also use ϕ to derive envelope masses, black hole masses, and black hole doubling times, and, lastly, we can derive mass loss rates and escape velocities from each of our fitted photospheres.

cases, we can see both layers at once only if the extended atmosphere has a non-unity covering fraction (see Section 4.3).

The available photon momentum bounds the outflow that supplies the extended atmosphere by $\dot{M}_{\rm wind} v_\infty \leq \eta L/c$, where η is the effective number of scatterings each photon undergoes before scattering down our line-of-sight, reaching 10–50 in optically thick outflows (H. J. G. L. M. Lamers & J. P. Cassinelli 1999). Given a hot component at $(T_{\rm h}, g_{\rm h})$ and a cool component at $T_{\rm c}$ on the same iso-ϕ line, we derive

$$\eta = \left(\frac{T_{\rm c}}{T_{\rm h}}\right)^2 \frac{3\,\kappa_{\rm es}\,\dot{M}_{\rm wind}^2\,c}{8\pi R_\star L}, \tag{10}$$

with $\dot{M}_{\rm wind}$ supplied by Equation (2) and $R_\star$ and L by the matching `MESA-QUEST` model (see Section 4.5).

Lastly, in Figure 2, we show a flowchart of all of the methods presented in this section. Reading from left to right, we begin with a spectrum of an LRD that we feed into our `Prospector` model, the latter of which includes both a host galaxy and a `TLUSTY` photosphere. We then use the fitted $(L, T_{\rm eff}, \log g)$ to derive ϕ, which we use throughout the rest of the manuscript to run quasi-star simulations and derive black hole masses and wind predictions.

4. RESULTS

4.1. *Photospheric Fits and Eddington Ratios*

We measure every ϕ in this paper from the fitted temperature and gravity alone, with no black hole mass, no bolometric correction, and no assumption about the power source, finding that almost every photosphere that we fit is super-Eddington. Table 1 lists our four fitted photospheres. Read as quasi-stars, the temperatures of our fitted photospheres are those of ordinary red giants, but their gravities sit below those of any known star. With our joint forward model that fits both the host galaxy and quasi-star simultaneously, we provide a solution to the overmassive black hole problem, showing that black holes at the centers of these objects sit at or below local scaling relations, even under the most conservative readings (see Section 4.3). M. C. Begelman et al. (2006) and M. C. Begelman et al. (2008) predicted objects of exactly this kind, black holes growing inside cool, low-gravity envelopes, nearly two decades before JWST found the first LRD, and our results provide models and simulations that indicate that we may indeed be watching the birth of intermediate-mass black holes (IMBH) with masses between 10^2–$10^5\,M_\odot$ (K. Inayoshi et al. 2020). We show the fit to WIDE-EGS-2974 in Figure 3 and the rest in Appendix C, and we release the chains for every fit in this paper.[8]

We fit The Egg with a single photosphere, reproduce its continuum and its atomic absorption lines, and constrain ϕ to the ten-percent level, finding that its photosphere radiates at hundreds of times its own Eddington limit. We also recover a $\phi > 100$ super-Eddington photosphere for The Rosetta Stone, which, according to virial mass estimates, historically had one of the largest virial masses in the LRD literature (I. Juodžbalis et al. 2024). As a quasi-star, it is much like The Egg—a low-mass, late stage, highly eruptive stellar envelope on its way

[8] https://github.com/o-curtis/lrd-quasistar-fits.

Table 1. Photospheric parameters and Eddington ratios of the fiducial fits. Here, the uncertainties show the spacings to the adjacent TLUSTY grid nodes. The GN-28074 uncertainties are expanded to include its degenerate young-host solution (see Section 4.4).

Source	Redshift	Component	$T_{\rm eff}$ (K)	$\log g$	[M/H]	ϕ
J1025+1402 (The Egg)	0.1007	single	4502^{+498}_{-2}	$-3.05^{+0.04}_{-0.06}$	-1	299^{+40}_{-26}
WIDE-EGS-2974	2.3203	hot	3710^{+290}_{-710}	$-1.51^{+0.23}_{-0.49}$	-1	$4.0^{+3.0}_{-1.7}$
		cold	2338^{+662}_{-338}	$-2.41^{+0.50}_{-0.44}$	-1	$5.0^{+7.9}_{-3.3}$
UNCOVER-A2744-20698	2.42	hot	3633^{+367}_{-633}	$-2.73^{+0.23}_{-0.27}$	-1	61^{+22}_{-15}
		cold	2338^{+662}_{-338}	$-1.59^{+1.35}_{-1.02}$	-1	$0.81^{+6.4}_{-0.77}$
GN-28074 (the Rosetta Stone)	2.26	single	4110^{+890}_{-110}	$-2.91^{+0.67}_{-0.09}$	-2	148^{+26}_{-115}

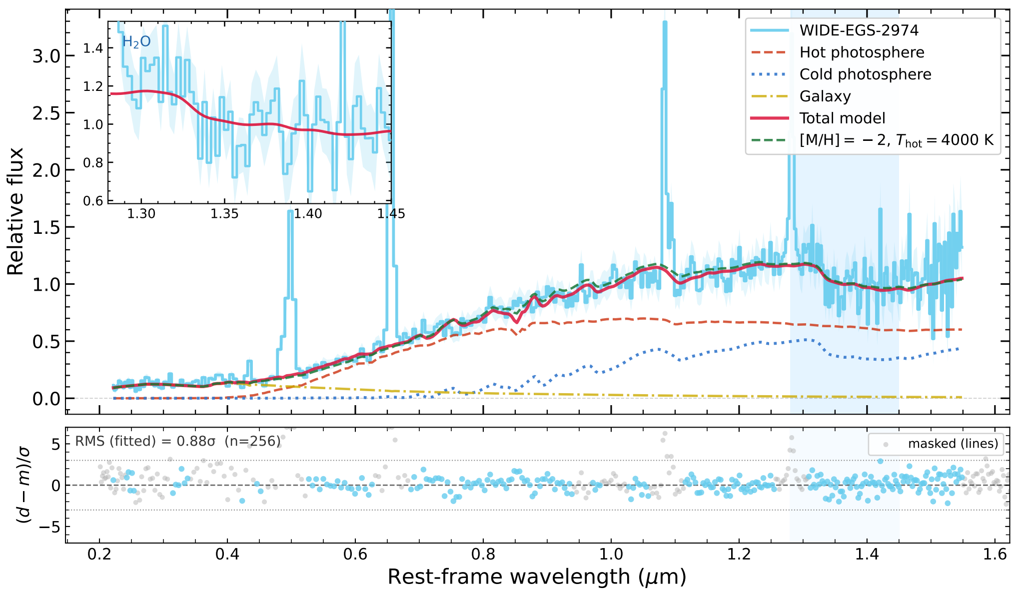

Figure 3. Our fiducial two-component fit to WIDE-EGS-2974 ($z = 2.32$). The light blue step curve is the NIRSpec PRISM spectrum with its 1σ uncertainty band shaded, the red dashed curve is the hot photosphere, the blue dotted curve is the cold photosphere, the gold dash-dotted curve is the host galaxy, and the crimson solid curve is the total model. The two photospheres share a single attenuation, and the cold component produces the water band. The lower panel shows the fit residuals in units of the uncertainty, with masked regions shaded gray. The light blue vertical band marks the 1.28–1.45 μm H_2O absorption region, which the inset enlarges. We note that the model wants to include Ca II triplet and Paschen series absorption, producing spurious features on the spectrum. This is purely a modeling constraint that only affects our water dot fits since our TLUSTY models do not include atmospheres with $[M/H] < -1$ at the temperatures that water absorption is possible. The dark green curve replaces the hot component with the library's closest metal-poor atmosphere ($[M/H] = -2$, which the grid provides only at 4000 K and above) that smooths these features while leaving ϕ unchanged. We also mask the emission features since our photospheric models are in local thermodynamic equilibrium (LTE) and contain no emission features.

to becoming a typical AGN (see Section 5.3). However, its spectrum (see Figure C3) still only shows tentative signs of a Ca II triplet at the current signal to noise, and it has a degenerate, lower ϕ, lower M_* solution that arises when we assume a different prior on M_* (see Section 4.4), so we treat its fit with the most caution.

The water dots prefer solutions with a second, colder surface that actually produces the water band itself. In WIDE-EGS-2974 we find that the two surfaces share a single Eddington ratio to within 0.1 dex, exactly as we predict would happen in an extended atmosphere (Section 3.4). We therefore interpret its cold component as the top of an extended atmosphere that covers the same energy source as the hot one with a covering fraction of ∼ 40% (Section 4.3). We fit WIDE-EGS-2974 as a quasi-star of mass 26,600 $M_\odot$, which is 40× and 2× higher than the masses that we derive for The Egg and The Rosetta Stone, suggesting that it has just recently transitioned off of its supermassive star phase where it is now starting to shed mass and grow its extended atmosphere (Section 5.3). A medium-resolution grating observation would resolve the blueshifted absorption of the outflow that supplies this atmosphere and directly measure our predicted outflow speed (Section 4.5). The cold component of UNCOVER-A2744-20698 instead fits at a gravity far above what any smooth outflow can supply, which we interpret as the water forming in a dense, pressure-confined cloud, or perhaps a starspot, that covers part of the star (see Section 4.2 for definitions of the terms). Higher resolution spectra may thus be able to deduce whether or not we are seeing clouds in the atmosphere of a quasi-star by resolving the water band into its individual lines, since a cloud moving with the outflow would shift those lines blueward of the photospheric absorption while a starspot would keep them at the stellar velocity.

4.2. *The ϕ-Conservation Test*

We find that the two components of WIDE-EGS-2974 share a single Eddington ratio within uncertainties, $\phi_{\rm hot}/\phi_{\rm cold} \approx 0.8$ with both values consistent at 1σ, the signature of an extended atmosphere (e.g., Equation (9)). Furthermore, their fitted luminosities agree to within 0.25 dex, their posteriors on $M_\bigstar$ overlap, and the cold photosphere sits at $1.9\,R_{\rm hot}$, all of which are again indicative of the cold component arising from an extended atmosphere that covers the same energy source as the hot component.

UNCOVER-A2744-20698 does not share this extended atmosphere behavior. Its hot component has $\phi = 61$ while its cold component fits at high gravity with $\phi = 0.8$. The cold spectrum requires photospheric pressures roughly 2.4 dex above what ϕ conservation predicts for an extended atmosphere, so the water in this source forms in a dense, cloud-like layer rather than at the top of a smooth atmosphere, much like the clouds that can form in the winds of super-Eddington outflows (N. J. Shaviv 2001) or in compact, pulsation-driven shells of material around the central engine (e.g., M. Cantiello et al. 2026; D. Nandal et al. 2026). We use the word cloud in its gas-phase sense, i.e., as a parcel of dense gas that is confined by the pressure of its surroundings, akin to how the clouds of the interstellar medium or broad-line regions of AGN (M. J. Rees 1987) are described, and not in the condensate sense as it is usually used in the substellar atmosphere literature (e.g., A. S. Ackerman & M. S. Marley 2001; B. E. Miles et al. 2023) since no condensate survives at these temperatures and pressures (H. R. Wakeford et al. 2017). For comparison, S. Takasao & K. Inayoshi (2026) already use "cloud" this way when defining their line-emitting plasma clouds that corotate in their model quasi-star magnetospheres. We note that starspots are a cool, magnetic alternative to clouds that would also cover part of the surface (Figure 1), but, due to the fact that they lie on the surface of the star, would require both components to have similar ϕ values, so we conclude that the cloud picture is the most likely interpretation for UNCOVER-A2744-20698.

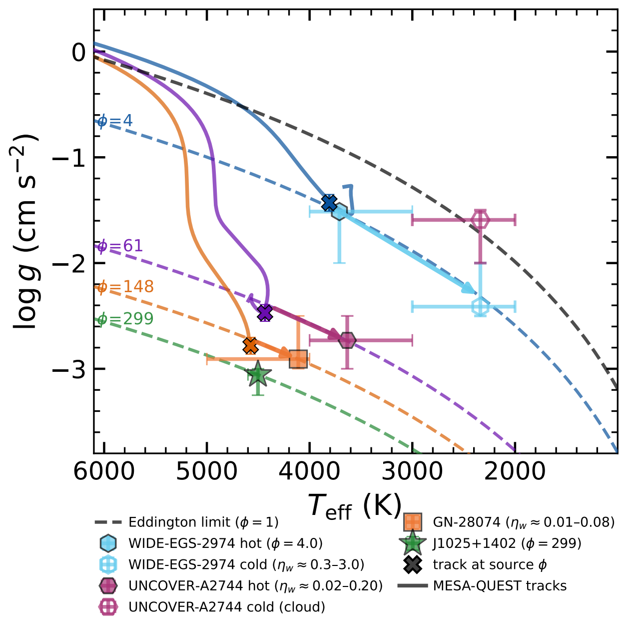

Figure 4. The results of our photospheric fits and `MESA-QUEST` simulations. Here, we plot all six fitted components as markers with grid-spacing error bars, the Eddington limit as the heavy dashed curve, and the four iso-ϕ lines as light dashed curves labeled at left. The solid curves are our converged `MESA-QUEST` evolutionary tracks. Each one enters hot from the upper left and settles onto the line of the source it was run for, and the cross marks the median of the track over that plateau. The vertical bar on each cross shows the twenty percent uncertainty in $f(Z)$ of Equation (5), which moves a quasi-star plateau up or down in $\log g$ at fixed $T_{\rm eff}$. Arrows show the wind shift along each iso-ϕ line. For WIDE-EGS-2974, the shift runs from the hot component to the cold one, and for GN-28074 and the UNCOVER-A2744-20698 hot surface it runs from the track crossing to the fitted photosphere. We give the momentum efficiency that each shift requires in the legend. Both high-$\alpha_{\rm acc}$ tracks stop soon after reaching their lines while the $\alpha_{\rm acc} = 4.6$ track runs on along its own, and our deep runs all terminate by $\phi \approx 160$–200 (see Section 3).

The extended atmosphere scenario thus naturally emerges from the WIDE-EGS-2974 data since both of its components lie on the same iso-ϕ line, but the cold component of UNCOVER-A2744-20698 instead prefers a $\log g$ value that is ~ 2 decades above its hot component. This seems to be a contradiction, since we usually infer $\log g$ as a proxy for the local gas pressure (I. Hubeny 1988; I. Hubeny et al. 2021), and a higher surface gravity would then imply that the cold component of UNCOVER-A2744-20698 has a higher gas pressure than its surroundings. While magnetic fields could provide this confinement (e.g., S. Takasao & K. Inayoshi 2026), as we discuss briefly in Appendix B, even modest magnetic fields only change our inferred surface gravities by $\lesssim 5\%$. At these low surface gravities (for reference, the surface pressures of our MESA-QUEST models are between 10^{-1}–10^{1} dyn cm^{-2} while the Sun has a surface pressure of 10^5 dyn cm^{-2}), magnetic pressure is possible but would need magnetic fields of order 10^2 G to raise $\log g$ by 2 decades, whereas the equipartition argument that we give in Paper II shows that these photospheres hold only gauss-level fields, enough to form starspots. We thus conclude that, while starspots cannot be ruled out, complete magnetic confinement is unlikely, so we interpret the cold component of UNCOVER-A2744-20698 as either a starspot or a dense, cold cloud, formed via ram pressure from shocked wind ejecta, that has a non-unity covering fraction, the latter of which could be possible if eruptive shocked ejecta compresses only part of the outflow (see Section 5.2).

We place all six photospheric components in the $T_{\rm eff}$–$\log g$ plane in Figure 4. We then run a MESA-QUEST simulation that aims at reproducing each of the hot photospheres, where we set the accretion factor from the measured ϕ and metallicity of each fit through Equation (5) (i.e., $\alpha_{\rm acc} \approx 4.6$ for WIDE-EGS-2974, $\alpha_{\rm acc} \approx 70$ for UNCOVER-A2744-20698, ≈ 152 for The Rosetta Stone at $[{\rm M/H}] = -2$, and ≈ 345 for The Egg). We use the seed masses of Section 3 and $\alpha_{\rm MLT} = 1.0$ throughout. These simulations do not, and are not intended to, reproduce the masses and luminosities of these objects. Equation (7) makes the iso-ϕ line that each track settles on independent of both, so tuning the models to reproduce $M_\bigstar$ and L precisely would not affect our results.

Each quasi-star enters hot from the upper left, cools as its black hole grows and its envelope settles, and lands on its own iso-ϕ line, where the crosses in the figure mark where it arrives and spends most of its time ($\approx$ Myr time scales). The WIDE-EGS-2974 track settles onto its line inside the grid uncertainties of the fitted hot component, and both WIDE components lie on that single $\alpha_{\rm acc} \approx 4.6$ line, which is the ϕ-conserved geometry of Section 3.4.

The iso-ϕ lines run parallel because ϕ sets g against $T_{\rm eff}^4$, so the vertical distance from any component down to the Eddington limit is $\log \phi$ itself. As discussed above, MESA-QUEST does not fully model how the outflow builds the extended atmosphere, but a growing atmosphere moves its photosphere down an iso-ϕ line towards cooler temperatures (e.g., Equation (9)) such that the difference between where the steady-state simulated photosphere lands and where the measured hot component sits informs us on the nature of the extended atmosphere itself. Lastly, we test the robustness of the simulations at high Eddington ratios by raising $\alpha_{\rm acc}$ until the models stop converging, finding that they fail at $\phi \approx 160$–200 depending on the mass and mixing length parameter used, which we interpret as the regime that is completely dominated by eruptive mass loss (see Section 5.2) such that a hydrostatic code can no longer follow it.

We find two sources that are cooler than the photospheres of the MESA-QUEST models with the same ϕ, which is itself a signature of an extended atmosphere. The Rosetta Stone track reaches its iso-ϕ line at 4548 K against a fitted 4109 K, and the hot surface of UNCOVER-A2744-20698 reaches its line at 4379 K against a fitted 3633 K. Any spherical outflow moves the $\tau = 2/3$ surface outward, cooling the observed photosphere and keeping the radiative layer beneath it hot such that the length of each arrow down an iso-ϕ line measures how far the extended atmosphere has expanded. WIDE-EGS-2974 needs no such shift on its hot component, whose track lands on the fitted marker since we already observe its cold and hot components separately (see above), so its arrow instead runs from the hot component to the cold one.

4.3. *The Mass Scale*

We now use our fits to calculate the total stellar masses, and, in doing so, individual black hole masses (E. R. Coughlin & M. C. Begelman 2024; J. B. Hassan et al. 2026). We write down the definitions of g, L, and $T_{\rm eff}$ for a spherical source, $g = GM_\bigstar/R_\bigstar^2$ and $L = 4\pi R_\bigstar^2 \sigma T_{\rm eff}^4$, where we assume $g = g_{\rm net}$ measured spectroscopically (Section 2.2), which give the stellar mass of the whole quasi-star as

$$M_\bigstar = \frac{\kappa_{\rm es} L}{4\pi G c\, \phi} = \frac{Lg}{4\pi G \sigma T_{\rm eff}^4}, \qquad (11)$$

We evaluate Equation (11) on the joint posterior of each source, allowing us to convert any fitted $(L, T_{\rm eff}, \log g)$ set into an estimate of the stellar mass, where, for our primary sources, our fits give $M_\bigstar = 682^{+65}_{-80}\, M_\odot$ for The Egg, $14{,}800^{+1{,}800}_{-2{,}300}\, M_\odot$ for The Rosetta Stone, $26{,}600^{+19{,}900}_{-11{,}500}\, M_\odot$ for WIDE-EGS-2974, and $5400^{+1800}_{-1400}\, M_\odot$ for UNCOVER-A2744-20698 at the hot-surface ϕ (Figure 5), where these uncertainties are statistical and Appendix B bounds the combined systematic at a factor of $\sim$2. For our two water dots, both of which prefer a 2-component fit, we sum together the fitted luminosities of both components. A fully opaque outflow would hide the hot surface entirely, so seeing two components at once, as is the case for WIDE-EGS-2974, requires the cold component to cover only part of the star, which we can use to derive a covering fraction for the extended atmosphere by conserving emitted power per unit solid angle as $f_{\rm cov} \equiv L_{\rm cold}/(L_{\rm hot} + L_{\rm cold}) = 0.37^{+0.06}_{-0.07}$ for this target.

The black hole mass follows from the interior structure of Section 3. A quasi-star cannot grow its black hole without limit since the envelope has to keep feeding the inner boundary and the structure fails once the hole has taken too much of the interior. Where that failure sits depends on how the inner boundary is posed. Bondi-type boundaries stall at a few percent (W. H. Ball et al. 2012), saturated-convection interiors run to 0.55–0.62 (E. R. Coughlin & M. C. Begelman 2024; A. D. Santarelli et al. 2026a), and the MESA implementation

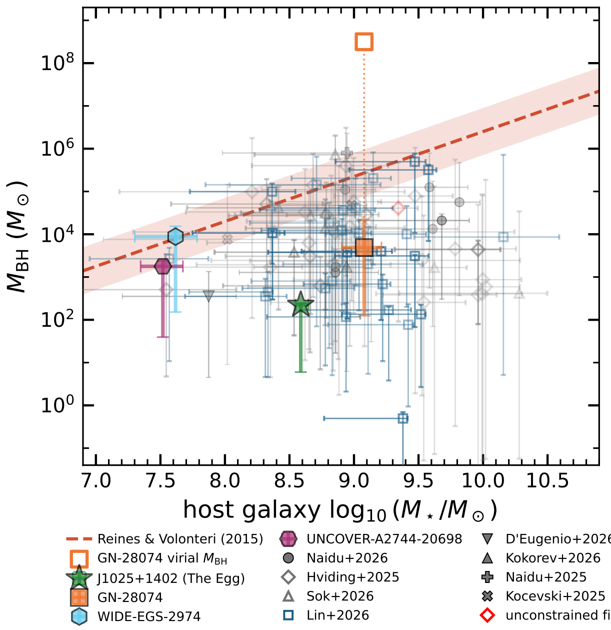

Figure 5. Black hole mass against host stellar mass, M_*. Read as quasi-stars, 77 of the 79 archival sources and three of the four primary sources are consistent with or well below the local relation, so no source requires an overmassive black hole. Filled markers show each source's quasi-star mass cap, $M_{\rm BH} = 0.33\,M_\bigstar$, at its fitted host mass, colored green for The Egg, purple for UNCOVER-A2744-20698, light blue for WIDE-EGS-2974, and orange for GN-28074. The blue pentagons are the DESI fits of X. Lin et al. (2026b), the best-constrained archival photospheres in our sample (Figure 6). The gray markers are the archival fits, with one marker shape per catalog as the legend lists. Each marker is the largest mass its black hole can have given the fitted photosphere. The upper error bars show the fitted uncertainties on $M_\bigstar$ while the single bar beneath it spans $M_{\rm BH} = 0.01$ to $0.33\,M_\bigstar$ (Section 4.3). Horizontal bars span the 16th to 84th percentiles of each fitted host mass, including the ~ 0.6 dex uncertainty that we add in quadrature to account for the effects that our priors have (e.g., Section 4.4). Even with these conservative error bars, every fit sits on or below the A. E. Reines & M. Volonteri (2015) relation—no overmassive black holes are required. Marker opacity scales with the rank of each posterior's quadrature width, so the best-constrained sources are darkest. The open square is the virial estimate for GN-28074. The dashed line and band show the local relation of A. E. Reines & M. Volonteri (2015) and its 0.55 dex scatter.

of J. B. Hassan et al. (2026) terminates at $M_{\rm BH}/M_{\rm rad} \approx 0.33$. We adopt the J. B. Hassan et al. (2026) value as the cap in Figure 5 since it is the most physically motivated, where each filled marker in that figure shows the maximum mass that the black hole could have (i.e., $M_{\rm BH} = 0.33 M_\bigstar$) with a bar that extends down to the few-percent Bondi-type stall at $0.01\,M_\bigstar$. Taking the saturated-convection ceiling would instead raise every cap by ~ 0.27 dex and taking a Bondi boundary would lower them by nearly a decade, but, still, neither choice moves a source out of the intermediate-mass range.

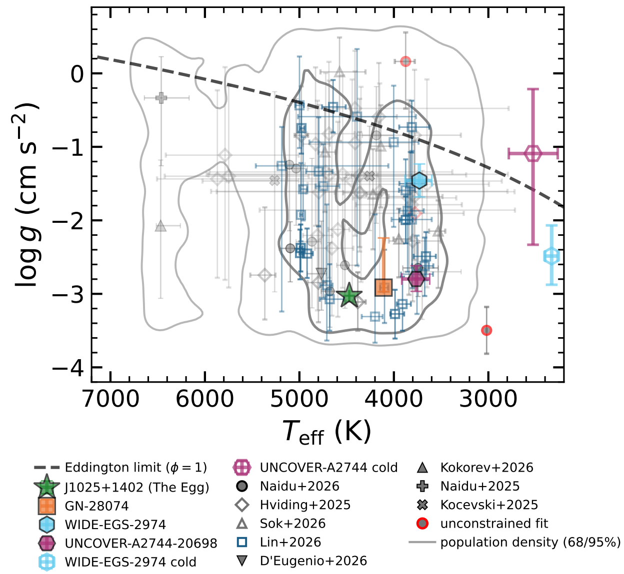

Figure 6. Fitted photospheric temperatures and gravities of all LRDs in this work, with the dashed line marking the Eddington limit $\phi = 1$ below which every source is super-Eddington. Colored markers are the four fiducial sources, with the open-faced hexagons as their fitted cold components. The blue pentagons are the DESI fits of X. Lin et al. (2026b). Gray symbols are the supplementary samples, circles for R. P. Naidu et al. (2026b), diamonds for R. E. Hviding et al. (2025), triangles for V. Sok et al. (2026), and the labeled downward and upward triangles for A2744-QSO1 and GLIMPSE-17775. Marker opacity scales with the rank of each posterior's quadrature width, so the best-constrained sources are darkest. Error bars span the 16th to 84th percentiles that have been added in quadrature with the 0.16 (0.32) dex spread in ϕ that our priors impose on the PRISM (DESI) fits (see Section 4.4). Bright red borders flag the three fits the text excludes as unconstrained. Contours enclose 68 and 95 percent of the stacked posterior density.

4.4. *The Population in the Photospheric Plane*

Figure 6 shows all of our fitted photospheres in the $T_{\rm eff}$–$\log g$ plane. Our 4 primary sources of interest are shown as colored markers, while our supplementary data are drawn in gray. Here, the contours show the inner 68% and 95% spread of the posterior mass, where we have excluded the cold components of the water dots and the unconstrained fits from their derivation. The photospheres concentrate at $T_{\rm eff} \approx 3800$–5000 K and $\log g \approx -2.7$ to -0.8, and 75 of the 82 median ϕ values sit on the super-Eddington side of the $\phi = 1$ line with the ensemble spanning $\phi \approx 0.1$–370. The relatively poor spectral resolution of PRISM causes the posteriors of many of these fits to be broad, but our sources still put ~ 82% of their posterior mass in the super-Eddington regime—5.4σ higher than the ~ 69% predicted by our priors alone which draw $T_{\rm eff}$ uniformly over 2000 to 6750 K and $\log g$ over -3.5 to $+0.5$. Even when we only keep the 28 sources whose ϕ posteriors span less than a decade, ~ 91% of their posterior mass sits above $\phi = 1$, which is 4.4σ above what our priors predict. Super-Eddington accretion thus seems to be a hallmark of the population that even PRISM-resolution spectra can pick up on.

We also note that these results are sensitive to the priors that we impose on our host galaxies. On average, our host galaxies are slightly more massive than what W. Q. Sun et al. (2026) derive by ~ 0.6 dex. When we refit each galaxy with a host that forms all of its stars within the last 30 Myr, we find no population-level change to our reported ϕ values within their quoted uncertainties. However, compared to our fiducial host masses, our refit galaxies end up being less massive by ~ 0.65 dex on average, aligning us with the population average of W. Q. Sun et al. (2026). These young-host refits move individual PRISM ϕ values by ~ 0.16 dex on median, while the DESI values move by ~ 0.32 dex, and we propagate these shifts into all of our figures which changes none of our results. Even with conservative uncertainties, almost all of our fitted LRDs are still consistent with being super-Eddington (Figure 6), and almost every quasi-star–host galaxy pair sits well below the A. E. Reines & M. Volonteri (2015) limit (see Figure 5).

We also perform injection recovery tests using real PRISM data. Here, we inject into the noise of 2 real PRISM spectra a sub- and super-Eddington photosphere at $(T_{\rm eff}, \log g) = (4500, -0.30)$ and $(4800, -2.65)$, or $\phi = 0.53$ and 152. The sub-Eddington injection provides the stronger test since our priors alone place 69% of their mass above $\phi = 1$. The recovered posterior is nearly the same in all four fits, spanning roughly 0.2 to 300 regardless of which target we inject, while the injected temperature is recovered every time. Repeating these injection recovery tests on real DESI noise returns $\phi = 2.5^{+1.3}_{-0.8}$ and 182^{+98}_{-61} for the sub- and super-Eddington injections, which recovers the super-Eddington value but overpredicts the sub-Eddington test. Even so, the only two sources whose posteriors sit fully below the Eddington limit are DESI sources.

4.5. *Predicted Wind Signatures*

In Table 2, we report limits on the wind signatures that an observer should expect from each source. Radiatively driven winds terminate near the escape speed (J. I. Castor et al. 1975; H. J. G. L. M. Lamers & J. P. Cassinelli 1999), so we report $v_\infty \approx (1\text{–}3)\, v_{\rm esc}$ using the fitted masses and radii. We derive η from Equation (10) using the difference in $\log g$ and $T_{\rm eff}$ between the `MESA-QUEST` result and the spectroscopy in the one-component case, and between the two spectroscopic components in the two-component case (Figure 4), and we take $\dot{M}_{\rm wind}$ from Equation (3). The Egg has no converged track as it sits in a super-eruptive regime that `MESA-QUEST` currently is unable to handle, so its row has a velocity estimate only. We derive the rates and efficiencies using Equation (3), so we quote them as upper limits. The velocities do not use that relation and follow from the escape speed alone.

Table 2. Expected wind signatures per source, showing the terminal speeds, mass loss rates, and wind efficiencies derived for each source (see text). To first order, these predictions already agree with the $\sim 200\text{–}1000\,{\rm km\,s^{-1}}$ blueshifted absorption edges that K. Park et al. (2026) derive (see also Table 3).

Source	v_∞ $({\rm km\,s^{-1}})$	$\dot{M}_{\rm wind}$ $(M_\odot\,{\rm yr^{-1}})$	η
The Egg	42–127	...	...
WIDE	260–770	0.11–0.33	0.3–3.0
UNCOVER	86–260	0.07–0.20	0.02–0.20
The Rosetta Stone	100–300	0.15–0.46	0.01–0.08

WIDE-EGS-2974 is thus a very interesting source, since it is the only source for which η can be inferred from two observed components with identical ϕ values. The difference in $T_{\rm eff}$ and $\log g$ for the two components fixes the ratio $\dot{M}_{\rm wind}/v_\infty$, such that $v_\infty \approx 933\,(\dot{M}_{\rm wind}/M_\odot\,{\rm yr^{-1}})\ {\rm km\,s^{-1}}$ and $\eta \approx 11\,(\dot{M}_{\rm wind}/M_\odot\,{\rm yr^{-1}})^2$, against the $0.1\,M_\odot\,{\rm yr^{-1}}$ and $100\ {\rm km\,s^{-1}}$ that the eruptive scheme of S. J. Cheng et al. (2024) gives at this mass scale. Resolving which wind scheme is correct thus requires $R \gtrsim 370$ at the fast end of the predicted range and $\gtrsim 550$ at its middle, so a single medium-resolution grating observation of the blueshifted Balmer absorption would measure v_∞ directly, and, since we can already fix $\dot{M}_{\rm wind}/v_\infty$, return the mass-loss rate itself.

5. DISCUSSION

Here, we have applied the quasi-star model to the black hole stars that lie at the center of LRDs (A. de Graaff et al. 2025a; R. P. Naidu et al. 2026a; W. Q. Sun et al. 2026), effectively testing the principles of stellar astrophysics on envelopes with radii $\sim 10^{16}$ cm and surface gravities $\log g \lesssim 0$. We fit their spectra with a series of `TLUSTY` stellar atmospheres and model their interiors with the stellar evolution code `MESA`. In doing so, we derive the relations that convert a fitted temperature and gravity into an accretion rate, a mass, and a mass-loss rate. Similarly to F. Gentile et al. (2026), we have made the quasi-star hypothesis testable on individual objects. We show that LRDs are consistent with envelopes akin to those seen in giant stars (similar to the pseudo-photosphere described in C. Ashall et al. 2026). That is, an extended atmosphere with molecular layers, clouds, and, as we will discuss in Paper II, a chromosphere and a corona (Figure 1; S. Höfner & H. Olofsson 2018; G. González-Torà et al. 2023, 2024). WIDE-EGS-2974 nearly confirms this structure by itself, since we observe both its hot surface and the top of its extended atmosphere in one spectrum.

No source in our sample requires an overmassive black hole, which we show for individual objects (Section 5.1). We can now start to interpret these results as an evolutionary sequence of quasi-stars (Section 5.3), and, in doing so, show that our results are consistent with the eruptive mass loss scheme of S. J. Cheng et al. (2024) and R. P. Naidu et al. (2026b). That is, our wind measurements separate the population into two regimes. The young, low-ϕ envelopes have outflows driven by their continua, while the older, least massive envelopes launch outflows at 1–3× their own escape speed (Section 5.2). With our `MESA-QUEST` simulations, we generate model quasi-stars that have the same ϕ as our fitted photospheres. Our tracks are also among the first quasi-star models evolved at a non-zero metallicity (see also J. Roman-Garza et al. 2026), where, compared to pristine simulations, the added metals cool and expand the photosphere (Section 5.1). Lastly, our fits return the first measured mass function for the population, where envelope mass falls with increasing ϕ (Section 5.3).

5.1. *The Mass Scale in Context*

Our mass measurements place all four sources at $M_\bigstar \sim 10^{2.8}$–$10^{4.4}\,M_\odot$ with black holes below a third of that (Figure 5; J. B. Hassan et al. 2026), squarely in the intermediate-mass regime that heavy-seed formation channels predict. Appendix B quantifies how these results depend on some of our underlying assumptions (e.g., the dynamical term $g_{\rm dyn}$, rotation, plane-parallel atmosphere models, and magnetic confinement), where we conclude that our masses are correct to within a factor of 2. Our biggest uncertainty is thus the fact that we only constrain black hole masses to be between $M_{\rm BH} \sim 0.01$–$0.33 M_\bigstar$ (e.g., E. R. Coughlin & M. C. Begelman 2024; J. B. Hassan et al. 2026), so future work is necessary to figure out how to distinguish where along its evolutionary track the quasi-star actually lives.

We also resolve the overmassive black hole problem, in which virial estimates place early black holes 10–100 times above the local $M_{\rm BH}$–$M_\bigstar$ relation (Y. Harikane et al. 2023; F. Pacucci et al. 2023). For instance, the virial estimate for The Rosetta Stone is $\log(M_{\rm BH}/M_\odot) \approx 8.5$ (I. Juodžbalis et al. 2024), which is $10^{4.8}$ times higher than the quasi-star mass cap that we place here. R. P. Naidu et al. (2026b) come to the same conclusion as us, where they discount virial estimates on the grounds that the lines form in a wind through bulk outflow motion and scattering.

Most of the bolometric luminosities in the literature are derived assuming that the line width is generated by the rotational motion around the black hole. For instance, I. Juodžbalis et al. (2024) convert the broad Hα luminosity of The Rosetta Stone into bolometric luminosities using the AGN calibration of J. Stern & A. Laor (2012), reporting a value that is an order of magnitude above our fitted photosphere ($\sim 10^{45}\,{\rm erg\,s^{-1}}$ vs. $\sim 10^{44}\,{\rm erg\,s^{-1}}$). J. E. Greene et al. (2026) have since measured the full X-ray to far-infrared output of two LRDs, finding that AGN corrections overestimate LRD luminosities by that same order of magnitude since LRDs show neither the X-rays nor the hot dust that the AGN correction factors assume. Using the correction described in J. E. Greene et al. (2026), the Hα-derived luminosity for The Rosetta Stone agrees with our fit. Under the assumption that the broad lines are rotationally broadened, I. Juodžbalis et al. (2024) derive a sub-Eddington accretion rate for The Rosetta Stone, whereas our mass measurements return $\Gamma_{\rm es}$ values in the hundreds regardless of whether we use our fitted luminosities or theirs.

The local relation between black hole and host stellar mass (A. E. Reines & M. Volonteri 2015), evaluated at our fitted host masses, predicts black hole masses that are a factor of 3.5 above the derived mass cap for UNCOVER-A2744-20698 and a factor of 1.1 below the WIDE-EGS-2974 cap, while The Egg and The Rosetta Stone fall 2.6 and 1.7 dex below the relation itself (Figure 5). In fact, as we show in Section 4.4, even when we refit every LRD with a host that forms all of its stars in a recent (< 30 Myr) starburst, the population still sits at or below the local scaling relation, and the few sources that rise above it remain consistent with the relation given its intrinsic scatter and the 0.01–0.33 $M_\bigstar$ range of each mass cap. Our fits thus return host stellar masses that we do not necessarily believe individually, though they are consistent with the halo masses implied by LRD environment and clustering measurements (Z. Pan et al. 2026; M. Carranza-Escudero et al. 2025; X. Lin et al. 2026c) as well as those derived from a host-galaxy decomposition of W. Q. Sun et al. (2026). That is to say, for our black holes to become overmassive, we would have to overestimate the host masses of The Egg and The Rosetta Stone, for example, by factors of ∼ 300 and 45, while even the maximally young host reading of Section 4.4 lowers the fitted host masses by only a factor of ∼4. We thus conclude that it is difficult to devise a scenario where a quasi-star, or even a black hole star in general, can produce an overmassive black hole. Our archival fits agree with these results, where we find that 75 of the 79 plotted masses fall below the relation, so no source in our sample requires an overmassive black hole, which is exactly the signal that we would expect to see if we truly are observing seeds that are caught partway through their initial growth phases.

One can also derive a mass from the continuum itself. For example, J.-R. Liu et al. (2026) model the red envelope as the photosphere of an optically thick outflow that is being driven by supercritical accretion, deriving masses between $M = 10^5$–$10^7\,M_\odot$ in a sample that includes The Egg. Their construction assumes that every source radiates at $L \approx (3/4)\,L_{\rm Edd}$, which gives $\phi \approx 0.75$ in our notation,

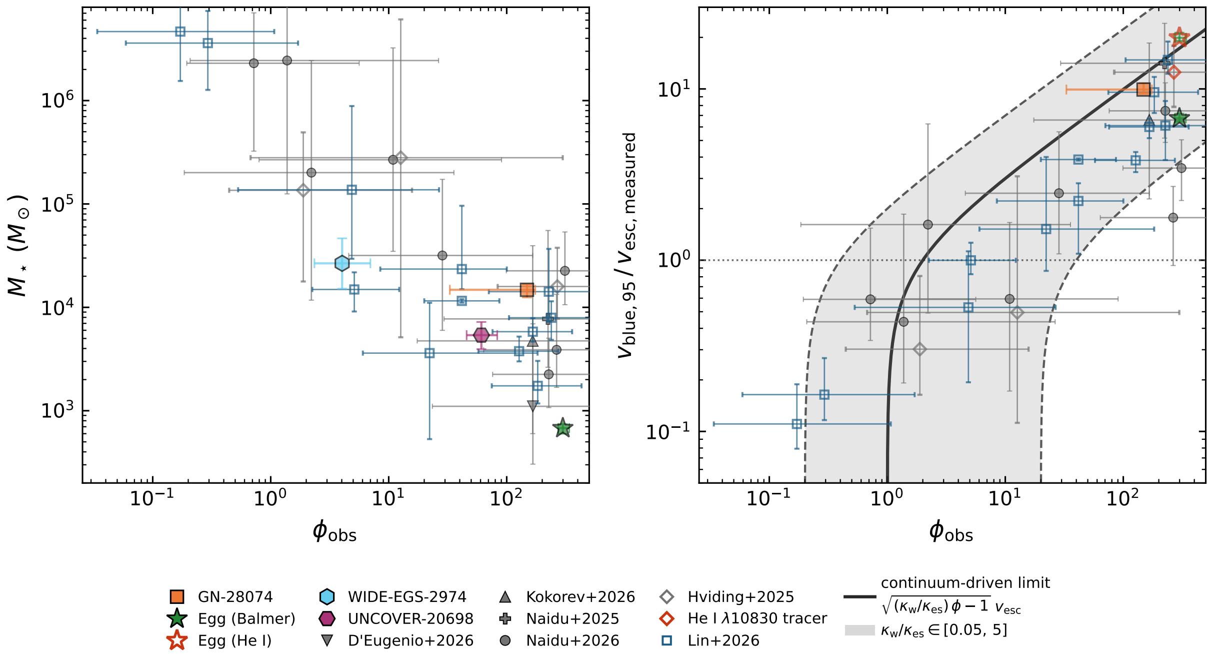

Figure 7. *Left:* the envelope mass from each source's own posterior through Equation (11), where the uncertainties show the posterior widths that have been added in quadrature with the $\sim$ 0.16–0.32 dex spread in ϕ that our choice of priors imposes (see Section 4.4). *Right:* $v_{\rm blue,95}$ that we derived from each source's transmission curve (see text and Figure 8), normalized by escape speeds that we derive from each fitted $(L, T_{\rm eff}, \log g)$. When paired with the left panel, we see that the quasi-stars with the lowest ϕ values have the most massive envelopes with slow winds, while late-stage quasi-stars have high ϕ values and thin, highly eruptive envelopes. The black line shows the continuum-driven limit that radiation dominated super-Eddington winds can drive (Equation (14)), similar to those seen in Wolf-Rayet stars and classical novae. The gray band varies the ratio between the opacity of the wind and the electron-scattering opacity to values comparable to those seen in the windless photospheres of our `MESA-QUEST` simulations on the low end and the outflows of line-driven winds on the high end. All of our measured sources are consistent with a radiation dominated, continuum-driven wind to within 1σ.

while our fitted photospheres return ϕ = 4.0–299. We instead fit the Ca II triplet and the molecular bands, whose depths respond to the photospheric pressure and therefore to the surface gravity.

Lastly, traditional quasi-star formation is thought to require metal-poor gas, but forming supermassive stars does not require it (e.g., S. Chon & K. Omukai 2020). Most existing models assume primordial gas (e.g., W. H. Ball et al. 2011; J. B. Hassan et al. 2026; A. D. Santarelli et al. 2026a) since supermassive star seeds must form in clouds that are too metal poor to fragment, but S. Chon & K. Omukai (2020) find that such stars can still form at metallicities as high as $\sim 10^{-3}\,Z_\odot$, especially when heated under external Lyman-Werner radiation (V. Bromm & A. Loeb 2003; J. A. Regan et al. 2016), and J. Roman-Garza et al. (2026) have evolved accreting quasi-stars at metallicities up to Z = 0.01 finding that their evolutionary tracks change little with Z. Several authors (e.g., S. F. Portegies Zwart & S. L. W. McMillan 2002; M. S. Fujii et al. 2024; F. Pacucci et al. 2025; A. Rantala 2026) have shown that runaway stellar collisions in dense star clusters can build supermassive stars of $\sim 10^4$–$10^5\,M_\odot$, which circumvents the traditional need to have quasi-stars form from a primordial gas cloud (e.g., M. C. Begelman et al. 2006). In fact, if supermassive stars form through such collisions, then quasi-stars should appear wherever young star clusters are forming, which is indeed the case since LRDs are as common at $z \sim 2$ as they are at $z \sim 5$ (S. Kapoor et al. 2026; F. Loiacono et al. 2026; X. Lin et al. 2026b), which agrees with the observed number densities of star clusters (J. Chisholm et al. 2026). We thus evolve our `MESA-QUEST` simulations at [M/H] = −1 with the AESOPUS opacities, and, while the added metals cool and expand the photosphere of an evolved quasi-star (Section 3), stable solutions do still evidently exist. A quasi-star accretes material from its host galaxy for the rest of its life (M. C. Begelman 2010; J. B. Hassan et al. 2026; A. D. Santarelli et al. 2026a), where it efficiently mixes with the rest of the envelope through convection. None of this changes our fitted masses; metallicity affects only our ϕ measurements (Equation (5)), while Equation (11) only uses the fitted temperature, gravity, and luminosity.

5.1.1. *Black Hole Doubling Times*

Equations (1) and (5) connect our inferred Eddington ratios ϕ to the black hole accretion factors $\alpha_{\rm acc}$, which we can use to determine how fast the central black hole of the quasi-star is assembling its mass. This is an important thing to consider in the context of supermassive black holes ($\sim 10^9\,M_\odot$) within the first billion years of the Universe's history, the so-called black hole seeding problem (e.g., K. Inayoshi et al. 2020; J. Regan & M. Volonteri 2024). Fundamentally, the problem relates to whether "light seeds" (i.e., $\sim$ 10–100 $M_\odot$ stellar remnants; P. Madau & M. J. Rees 2001) or "heavy seeds" ($\sim 10^4$–$10^5\,M_\odot$ direct-collapse objects; V. Bromm & A. Loeb 2003) are responsible for the first supermassive black holes. Light seeds require smaller initial masses but faster doubling times in order to produce the observed supermassive black hole masses at later times, whereas heavy seeds require larger initial masses but fewer doublings (e.g., R. Maiolino et al. 2024; Á. Bogdán et al. 2024). Quasi-stars are an example of a heavy-seed channel that grow their black holes at a rate that is proportional to the mass of the entire envelope (M. C. Begelman et al. 2006, 2008; J. B. Hassan et al. 2026; A. D. Santarelli et al. 2026a).

We can estimate the black hole doubling time of our sources using our fitted ϕ and $M_\star$ values. Following E. R. Coughlin & M. C. Begelman (2024) and M. C. Begelman & J. Dexter (2026), we start with the definition of the black hole growth rate from Section 3, i.e., $\dot{M}_{\rm BH} = (1-\varepsilon)L_{\rm BH}/(\varepsilon c^2)$ for radiative efficiency ε that we again assume to be 0.1. We also assume that the energy lost to winds is negligible (see Appendix B) such that the envelope completely reprocesses the accretion luminosity, giving $L \approx L_{\rm BH}$. If we integrate this relation from time $t = 0$ when the black hole has mass $M_{\rm BH}$ to the instantaneous doubling time $t = t_{\rm double}$ when the black hole has mass $2M_{\rm BH}$, we find that $t_{\rm double} = \frac{M_{\rm BH}}{\dot{M}_{\rm BH}}$ (E. R. Coughlin & M. C. Begelman 2024; M. C. Begelman & J. Dexter 2026). Equation (11) then gives the total mass of the quasi-star as $M_\star = \frac{\kappa_{\rm es} L}{4\pi G c \phi}$, which J. B. Hassan et al. (2026) relate to the black hole mass by $M_{\rm BH} \leq 0.33 M_\star$, so we are left with the inequality

$$t_{\rm double} = \frac{M_{\rm BH}}{\dot{M}_{\rm BH}} \leq 0.33\,\frac{\varepsilon}{1-\varepsilon}\,\frac{\kappa_{\rm es}\,c}{4\pi G}\,\frac{1}{\phi} \approx 14\,\phi^{-1}\ \text{Myr}. \quad (12)$$

The Egg, for instance, has $\phi \sim 300$ and will thus double its black hole mass in $\sim$ 50 kyr, while WIDE-EGS-2974, which has $\phi \sim 4$, will double in $\sim$ 3.5 Myr. In general, these doubling times range from ~0.5–3.5 Myr for our $\phi \lesssim 30$ sources and ~0.05–0.5 Myr for our $\phi \gtrsim 30$ sources.

In the absence of outflows, the final masses of these objects are expected to be $\sim 10^2$–$10^4\,M_\odot$, approaching the heavy seed scenarios. While winds can strip the envelopes of our highest-ϕ sources on the order of 10^4 years (see Appendix B.1), the presence of inflowing material can resupply their envelopes, offsetting the rate of mass loss (e.g., A. D. Santarelli et al. 2026a; J. Roman-Garza et al. 2026). In the context of the evolutionary sequence that we discuss in Section 5.3 below, the young, low-ϕ, high envelope mass sources double slowly but still have a lot of envelope to either accrete onto their black hole or blow away, while the late-stage, high-ϕ, lower envelope mass sources are both growing their black holes and expelling their envelopes at much faster rates.

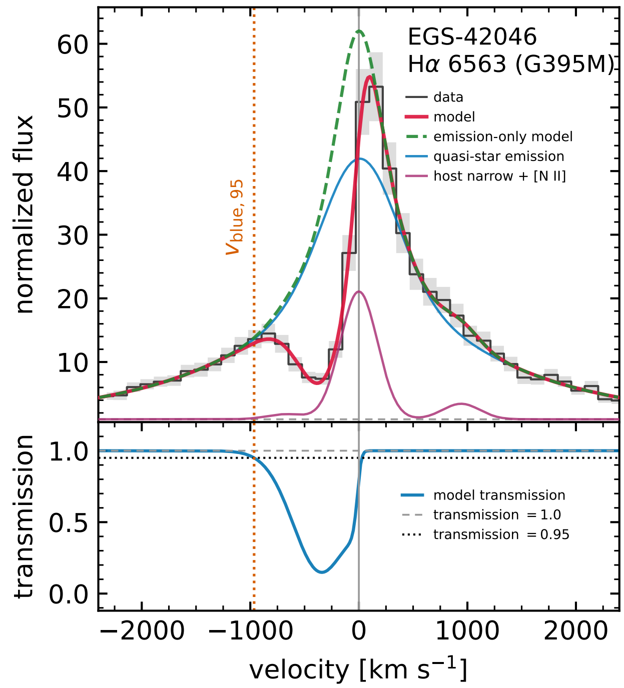

Figure 8. Our $v_{\rm blue,95}$ measurement for RUBIES-EGS-42046. The top panel shows RUBIES-EGS-42046's G395M grating spectra of the continuum-normalized Hα (solid black) with the best-fit model of J. Matthee et al. (2026) (solid red; see text), the emission-only model that includes the narrow emission from the host as well as the narrow and broad emission from the quasi-star (dashed green), the quasi-star's emission (solid blue), and the host galaxy's narrow Hα and [N II] emission (solid purple). The bottom panel divides the total model by the emission-only model to produce a transmission curve that represents the total fraction of quasi-star light that has not been absorbed (solid blue). The dotted orange marks $v_{\rm blue,95}$, i.e., the blueshifted velocity edge of the absorption trough where the transmission curve returns to 95% of its systemic value.

5.2. *Winds Across the LRD Population*

We now extend our wind analysis beyond our 4 primary sources. From here on, we refer to a source as "molecularly veiled" when cool material covers its photosphere and imprints molecular absorption (e.g., water absorption) on the spectrum. Molecular veiling requires the outflow to stay optically thick out to the radius where it cools below the ~2500–3000 K that water chemistry needs. At fixed momentum efficiency, high-ϕ sources drive fast, optically thin winds that should rarely veil, while moderate-ϕ sources with dense outflows could veil completely. This agrees with our sample. The water-veiled WIDE-EGS-2974 sits at $\phi \approx 4$, the cloud-veiled UNCOVER-A2744-20698 at $\phi \approx 61$, and The Rosetta Stone and The Egg, which show bare atomic photospheres with Ca II absorption and no molecular bands, sit at $\phi \approx 148$

and 299. Molecular absorption should therefore concentrate at low ϕ and high $\dot{M}_{\rm wind}$ while the highest-ϕ LRDs should appear as bare ~5000 K photospheres. However, the majority of our sample still shows outflow signatures in their lines, where Balmer photons scatter far outside the continuum photosphere and imprint blueshifted absorption near v_∞ together with the electron-scattering wings that dominate LRD Balmer profiles (R. P. Naidu et al. 2026b).

In Figure 7, we investigate the mass functions and wind signatures across our sample. The left panel shows how our derived envelope masses vary as a function of ϕ, where we see that the population median is $\sim 10^4 M_\odot$. These were calculated with Equation (11), which shows that $M_\bigstar \propto L/\phi$, so the downwards trend is mostly a tautology. Still, we will show below that the least massive sources drive the most eruptive winds, while the most massive sources drive slower, continuum-driven outflows.

We first use each of our fitted (L, $T_{\rm eff}$, $\log g$) values to calculate the escape velocity of each source as $v_{\rm esc} = \sqrt{2GM_\bigstar/R_\bigstar}$. After subtracting the continuum from our spectra, we follow J. Matthee et al. (2026) to model the absorbed Balmer profiles of our lines (see Figure 8 for an example of this decomposition for the Hα line of RUBIES-EGS-42046). Using Equation 1 from their paper, we model each of our line profiles as the sum of the emission from the quasi-star that gets partially broadened by electron scattering and absorbed by a skewed-Gaussian absorber, along with the host galaxy's unabsorbed narrow-line component, which, in the case of our region near Hα, includes the [N II] $\lambda\lambda$6548, 6583 narrow-line doublet. All of this is then convolved with the line-spread function of the instrument. The bottom panel of this figure then shows the ratio of the total model divided by the emission-only, producing a transmission curve that measures the fraction of light that was not absorbed at a particular velocity. Following R. P. Naidu et al. (2026b), we then calculate $v_{\rm blue,95}$, i.e., the blueshifted velocity edge of the absorption trough where the transmission curve returns to 95% of its systemic value, which we take to be representative of the fastest material that is being launched by each source's wind.

In the right panel of Figure 7, we plot $v_{\rm blue,95}/v_{\rm esc}$ vs. ϕ, where a value > 1 (dashed gray line) indicates that the wind is being launched at a speed greater than its escape velocity. When paired with the left panel, we see that it is the slow, near-systemic absorbers that have the largest masses and the lowest ϕ values, while the least massive, highest ϕ sources expel extremely eruptive winds. The Rosetta Stone, for instance, has a total mass of $\sim 10^4 M_\odot$ and ejects material at nearly 10× its escape velocity. For most of the sources in our sample, the relationship between $v_{\rm blue,95}/v_{\rm esc}$ and ϕ very closely follows the continuum-driven limit that radiation dominated super-Eddington winds can drive (N. J. Shaviv 2001; S. P. Owocki et al. 2004; A. J. van Marle et al. 2008; E. Quataert et al. 2016). We show this relation in the right panel, where we assume $v_\infty \approx v_{\rm blue,95}$ under the assumption that $v_{\rm blue,95}$ traces the fastest outflowing material of the wind (see also R. P. Naidu et al. 2026b). To derive this relation, consider the fact that the conservation of momentum for a radially symmetric wind dictates that

$$v\frac{dv}{dr} = -\frac{GM}{r^2} + \frac{\kappa_{\rm w} L}{4\pi r^2 c}, \tag{13}$$

where the first and second terms on the right hand side are the gravitational acceleration and the outwards radiative acceleration for a wind with opacity $\kappa_{\rm w}$, respectively. Integrating from positions $r = R_\bigstar$ where the wind has velocity $v = 0$ to $r = \infty$ where the wind has velocity v_∞ and substituting in the definitions for $v_{\rm esc}^2 = \frac{2GM_\bigstar}{R_\bigstar}$ and $\phi = \frac{\kappa_{\rm es} L}{4\pi GM_\bigstar c}$ gives

$$\frac{v_\infty}{v_{\rm esc}} = \sqrt{\frac{\kappa_{\rm w}}{\kappa_{\rm es}}\phi - 1}, \tag{14}$$

which others have also derived in the context of super-Eddington winds in Wolf-Rayet stars and classical novae (e.g., N. J. Shaviv 2001; S. P. Owocki et al. 2004; A. J. van Marle et al. 2008; E. Quataert et al. 2016). The gray band in Figure 7 varies the $\kappa_{\rm w}/\kappa_{\rm es}$ opacity ratio between 0.05–5. The lower bound is comparable to the opacities that our windless `MESA-QUEST` photospheres arrive at, while the upper bound represents winds with opacities > $\kappa_{\rm es}$, which is common in line-driven winds (J. I. Castor et al. 1975). Every source is consistent with this continuum-driven framework to within 1σ.

Our archival fits also reveal gas that is redshifted rather than blueshifted, which aligns with our interpretation in Figure 1 that draws the photosphere as the interface between a free-falling inflow and an extended atmosphere akin to those seen in AGB stars (see also Figure 1 of C. Ashall et al. 2026 who devises a similar geometry to ours). The Egg, for instance, has an Hβ absorber that is redshifted to +73 km s^{-1} along with its other blueshifted wind lines, which we interpret as the settling of some of the material as it falls back onto the photosphere.

5.3. *An Evolutionary Sequence for the LRD Population*

Our measurements suggest an evolutionary sequence within the LRD population. Figure 7 shows that the most massive envelopes have the lowest Eddington ratios and sit on the continuum-driving band, while the least massive envelopes have the highest Eddington ratios and launch at their own escape speed. Across the 27 sources with measured absorbers, envelope mass falls with increasing ϕ. Equation (11) makes $M_\bigstar \propto L/\phi$, so part of this trend is the definition itself, but further testing has revealed that the source luminosities do not trend with ϕ (Section 5.2), so the decline reflects a real spread in ϕ at fixed luminosity rather than the definition alone.

Table 3. Observable predictions of the quasi-star framework from our fitted photosphere parameters, the measurements that test them, and where each test stands as of this work.

Observable	quasi-star expectation	Test and requirement	Status
Mass scale	Envelope masses can be derived with $M_\bigstar = \kappa_{\rm es} L/(4\pi G c\ \phi)$ and black hole masses with $M_{\rm BH} \leq 0.33\, M_\bigstar$ (Equation (11)). No overmassive black holes are required	Population-level photospheric fits with better constrained host masses	ϕ measured for 86 sources (Sections 4.4 and 4.3)
Wind velocities	Winds off the photosphere launch at either a rate proportional to their continuum emission or as 1–3 $v_{\rm esc}$ for eruptive winds (Figure 7)	Photospheric fit plus one grating measurement	Measured for 27 sources, with 14 at or below 3 $v_{\rm esc}$ and 25 inside the band (Section 5.2)
Eddington-ratio conservation	Extended atmospheres conserve ϕ. When covering fractions are < 1, their cold and hot components sit on an iso-ϕ line (Section 3.3)	Two-component photosphere fits	Confirmed for WIDE-EGS-2974. UNCOVER-A2744-20698 has a denser cold component. None of our archival fits prefer a cold component. (Section 4.4)
Derived mass-loss rates	The shift down an iso-ϕ predicts mass loss rates and terminal velocities (Section 4.5)	One NIRSpec G395M observation at $R \approx 1000$, resolving the water band at 4.3–4.8 μm	Predicted for a few sources, notably WIDE-EGS-2974 which has a hot and cold component on an iso-ϕ line.
Molecular veiling	Cold, low-ϕ sources have molecularly veiled envelopes, while the hottest, highest-ϕ LRDs are bare ~5000 K photospheres (Section 5.2)	Photospheric fits across the entire population	Holds in this sample of ~ 80 LRDs

We interpret this as an age sequence. A quasi-star begins with most of its birth envelope still in place, so the envelope is massive, less luminous, and its outflows are continuum-driven (A. D. Santarelli et al. 2026a,b). Winds progressively strip the envelope while the luminosity remains constant, so ϕ climbs and the winds become eruptive (S. J. Cheng et al. 2024; R. P. Naidu et al. 2026b). Our four primary sources sample both ends of that track; WIDE-EGS-2974 is the most massive at 26,600 $M_\odot$ but it has the lowest Eddington ratio at $\phi = 4.0$ and its predicted wind speed (Table 2) is consistent with both the eruptive and continuum-driven schemes. The Egg, on the other hand, is one of the least massive sources in our sample at 682 $M_\odot$, but its envelope is extremely super-Eddington at $\phi = 299$, which places it squarely in the eruptive outflow regime of Figure 7. J. B. Hassan et al. (2026) come to the same conclusion, where they find that their eruptive mass loss begins early, peaking at mid-evolution, and ceases as the envelope thins. Similarly, Z. Stone et al. (2026) claim that the coolest LRDs with $T \lesssim 3000$ K appear only at $z \lesssim 4$, which they interpret as a transitional stage of the population.

One of the successes of this framework is that it does not require holes or funnels that extend down to traditional broad-line regions in the vicinity of the black hole (e.g., J.-R. Liu et al. 2026; P. Madau & R. Maiolino 2026; X. Ji et al. 2026; M. Tang et al. 2026). Such channels would imprint a viewing-angle dependence on the population, but such dependencies must be minor, since LRDs as a population seem mostly homogeneous (A. de Graaff et al. 2025a). These holes are also unstable in the envelopes that we simulate, where the free-fall and convective timescales are only decades long. A sustained wind or a strong magnetic field could hold a channel open, but, as we discuss in Paper II, an equipartition argument can reveal that these photospheres can only sustain Gauss level fields at most. The covering fractions that our fits measure are therefore gaps in the extended atmosphere that expose the radiative layer below.

Still, the quasi-star phase must end at some point to give way to an AGN and quasar population, which means that, at some point, sightlines to the interior should open up. J. B. Hassan et al. (2026) predict that the quasi-star envelope destabilizes at $M_{\rm BH}/M_{\rm rad} \approx 0.33$, which takes $\sim$ 1–20 Myr depending on mass-loss rate and accretion rate (A. D. Santarelli et al. 2026b; J. B. Hassan et al. 2026). M. C. Begelman & J. Dexter (2026) described this transitional period in late-stage quasi-stars as an ionized atmosphere with scattering depths of 10–20, and several authors (e.g., F. Pacucci & R. Narayan 2024; H. Liu et al. 2025; E. Lambrides et al. 2026) have characterized the final stages as a super-Eddington accretion flow, i.e., a geometrically thick disk or quasi-spherical inflow whose surface radiates at the local Eddington limit. As the mass loss continues, the continuum will start to fade and X-rays and high-ionization lines will start to travel through the atmosphere as the covering fraction falls. R. E. Hviding et al. (2026) may have already detected such a transition point with the detection of X-rays emanating from an LRD-like object. Similarly, the two "forges" of S. Fu et al. (2026) show both the characteristic V-shape spectrum and the X-ray, radio, and hot-dust emission of quasars. The almost negligible X-ray detection rate implies that this transitory state is rare, even as the LRD number density itself stays roughly flat from $z \sim 5$ to $z \sim 2$ before declining toward lower redshift (S. Kapoor et al. 2026; F. Loiacono et al. 2026).

6. CONCLUSION

We fit low-gravity TLUSTY photospheres with host galaxies to the four LRDs with the strongest known absorption features, at $z = 0.1$–2.4, as well as to 82 archival JWST and DESI sources. For each, we calculate the Eddington luminosity ratio $\phi = \kappa_{\rm es}\sigma T_{\rm eff}^4/(g_{\rm net}c)$, which we use to derive accretion rate factors, black hole and envelope masses, and escape velocities.

1. Most of our sources exhibit super-Eddington accretion ratios, with our four primary sources spanning $\phi = 4$–299. All of these correspond to masses between 700–27,000 $M_\odot$. Along with the fitted host galaxy stellar masses, we show that no LRD requires an overmassive black hole; we conclude that we are instead observing supermassive black hole seeds.

2. In the quasi-star scenario, we map the fitted Eddington luminosity ratios to the accretion factor $\alpha_{\rm acc}$ that we use to run `MESA-QUEST` simulations of each object out to its radiative layer. We have thus made a self-consistent framework that allows us to test the quasi-star hypothesis as a potential central engine for LRDs, where, for the first time, we provide a single, falsifiable model and show that our model is fully consistent with the energy budget that is transported through quasi-stars.

3. Similarly, we connect ϕ to the black hole accretion rates, finding that the doubling time of the black hole at the center of a quasi-star is roughly $t_{\rm double} \leq 14\,\phi^{-1}$ Myr. Our results indicate that the black holes in the centers of quasi-stars double on timescales of ∼0.05–3.5 Myr and are more than capable of satisfying the heavy-seed scenario, especially in the presence of inflows that resupply their envelopes (e.g., A. D. Santarelli et al. 2026a; J. Roman-Garza et al. 2026), producing IMBHs within the quasi-star lifetime.

4. We derive escape velocities for all of our objects, which we compare against measured blueshifted absorption features. High-ϕ, low-mass sources eject material at 1–3× their escape velocities, while low-ϕ, high-mass sources are continuum driven. We interpret this as an evolutionary sequence for LRDs. Recently formed quasi-stars with massive envelopes have low Eddington luminosity ratios, slow winds, and long black hole doubling times, while late-stage quasi-stars have thin, eruptive envelopes and faster black hole doubling times.

5. Two of our sources show water absorption in their spectra, which necessitates a two-component fit to their data. The hot and cold components of WIDE-EGS-2974 share a ϕ value, fully consistent with our ϕ-conservation test, implying that its water forms at the top of an extended atmosphere. UNCOVER-A2744-20698 instead has a cold-component that is 2 dex denser than its hot-component, which we interpret as material in a dense cloud.

JWST first discovered LRDs within its first year of operations, yet all aspects of their nature, from their broad emission lines, their v-shaped UV-optical spectrum, and their lack of X-ray emission, remain challenging for any single model to describe. And yet, M. C. Begelman et al. (2006) and M. C. Begelman et al. (2008) first proposed the quasi-star as a possible solution to the supermassive black hole seeding problem nearly two decades before LRDs were widely discovered. Here, we have shown that the defining characteristics of LRDs can consistently be described as originating from the photospheres and extended atmospheres that surround quasi-stars. No LRD in our sample hosts an overmassive black hole, and we have shown that LRDs may provide evidence that heavy seeds, rather than light stellar-remnant seeds, may have produced the supermassive black holes and quasars that we see within the first billion years of the Universe's history (e.g., R. Maiolino et al. 2024). That is, we may be observing supermassive black hole seeds. Table 3 summarizes all of the tests that we performed throughout this manuscript. A natural extension of this work is a non-hydrostatic equilibrium numerical simulation, such as a 3D radiation magnetohydrodynamic simulation of a quasi-star's atmosphere and extended envelope that is capable of resolving the convective flux transport, line profiles, eruptive mass launching, and clouds that a hydrostatic solver like `MESA` cannot model.

ACKNOWLEDGEMENTS

O.C. acknowledges support as a Penn State Extraterrestrial Intelligence Center Postdoctoral Fellow, which is funded through a private donation made by The Ultraintelligence Foundation. O.C. would like to thank Rohan Naidu whose comments helped strengthen this manuscript. O.C. would like to thank Xiaojing Lin for sharing the reduced LBT/MODS and Magellan/FIRE data of The Egg that we used in this analysis.

Portions of the code used in this work were developed with Claude Code, a subscription to which was paid for by Penn State's Institute for Gravitation and the Cosmos. All of the analysis, text, and claims herein are strictly our own. This research was partially supported by the Seed Grant award ICDS_READ26_m1jtw13 from Penn State's Institute for Computational and Data Sciences. The Penn State Extraterrestrial Intelligence Center and the Center for Exoplanets and Habitable Worlds are supported by Penn State and its Eberly College of Science. This research has made use of NASA's Astrophysics Data System Bibliographic Services. We performed all computational work on the Roar Collab supercomputer, administered by Penn State's Institute for Computational and Data Sciences.

J.M.H. acknowledges support from the Evolving Universe Fellowship, which is made possible by a generous donation from Dr. Keiko Miwa Ross. J.M.H. also acknowledges support from JWST Program #8544.

Some of the data products presented herein were retrieved from the Dawn JWST Archive (DJA). DJA is an initiative of the Cosmic Dawn Center (DAWN), which is funded by the Danish National Research Foundation under grant DNRF140. We retrieved the JWST observations from the Mikulski Archive for Space Telescopes, where the WIDE survey is archived at 10.17909/57km-j134, UNCOVER at 10.17909/zn4s-0243, and JADES at 10.17909/8tdj-8n28.

Facilities: JWST(NIRSpec), LBT(MODS), Magellan:Baade(FIRE), Mayall(DESI)

Software: `MESA` (B. Paxton et al. 2011; A. S. Jermyn et al. 2023), `MESA-QUEST` (C. B. Campbell et al. 2025; A. D. Santarelli et al. 2026a), `TLUSTY` (I. Hubeny 1988; I. Hubeny et al. 2021), `Prospector` (B. D. Johnson et al. 2021), `FSPS` (C. Conroy et al. 2009), `dynesty` (J. S. Speagle 2020), `AESOPUS` (P. Marigo & B. Aringer 2009), `astropy`, `numpy`, `scipy`, `matplotlib`, `sedpy`, Claude Code (Anthropic).

APPENDIX

A. THE LOCAL EDDINGTON STRUCTURE OF THE MATCHED MODELS

In this appendix, we measure the local Eddington ratio $\Gamma_{\rm rad}(r)$ of Equation (6) using our `MESA-QUEST` models to show that the radiative layers of our simulated quasi-stars are indeed sub-Eddington. As a reminder, `MESA-QUEST` is a hydrostatic code, so all of our simulated objects are sub-Eddington by definition. Still, there are regions in the envelope that have $\Gamma_{\rm rad} > 1$, which creates density inversions that ultimately drive the eruptive mass loss (see, e.g., S. J. Cheng et al. 2024; J. B. Hassan et al. 2026; M. C. Begelman & J. Dexter 2026 for more detail on eruptive mass loss schemes). `MESA-QUEST` is only able to model out to the radiative layer of Figure 1, so "photosphere" in this Appendix refers to this simulated photosphere (whose radius is $R_{\rm rad}$), not to the top of the extended atmosphere that we describe in the main text (whose radius is $R_\bigstar$). We show in Section 3.4 that ϕ is conserved between these two surfaces, so below, we use our fitted ϕ values from the main text.

We evaluate Equation (6) at the photosphere. There, $\Gamma_{\rm rad} = \phi\,\kappa_{\rm rad}/\kappa_{\rm es}$ where $\kappa_{\rm rad}$ is the photospheric Rosseland mean opacity that we calculate from our simulations and $\kappa_{\rm es}$ is the electron-scattering opacity. Figure A1 shows the resulting ratios. Each of our simulated photospheres sits below its local Eddington limit.

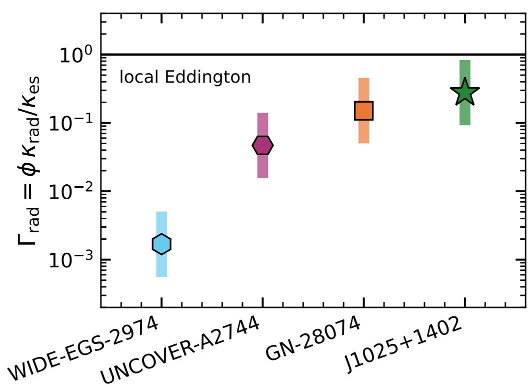

Figure A1. Local Eddington ratio at our simulated photospheres, with $\kappa_{\rm rad}$ derived from our `MESA-QUEST` simulations and ϕ from our spectroscopic fits. The horizontal line marks the local Eddington limit. Every simulated photosphere sits below its local Eddington limit, implying that the outflows launch below the photosphere (Section 3.3).

We show the internal structure of a `MESA-QUEST` simulation in Figure A2 through a converged $\alpha_{\rm acc} = 13.5$ model at $M_{\rm BH}/M_{\rm rad} = 0.10$ (where $M_{\rm rad}$ is the total mass interior to the radiative layer) and $T_{\rm eff} = 4109$ K. Deep in the envelope, the radiative flux sits at the local Eddington value. The shaded band shows where $\Gamma_{\rm rad}$ exceeds unity, which leads to a density inversion. Outside the band, the opacity tends towards $\kappa_{\rm rad} \approx 10^{-4}\,{\rm cm^2\,g^{-1}}$ and the model's surface sits at $\Gamma_{\rm rad} \approx 5 \times 10^{-3}$, locally sub-Eddington. The temperature panel shows the same structure, where the $\tau = 1$ layer is $\sim 6\%$ hotter than the $\tau = 2/3$ surface, implying limb-darkening across the photosphere.

We then derive a launch criterion for the atmosphere. That is, we derive the condition for which any outgoing pressure cannot be contained by the weight of the atmosphere above it. To do this, we first compute the gas pressure $P_{\rm gas}$ and the radiation pressure

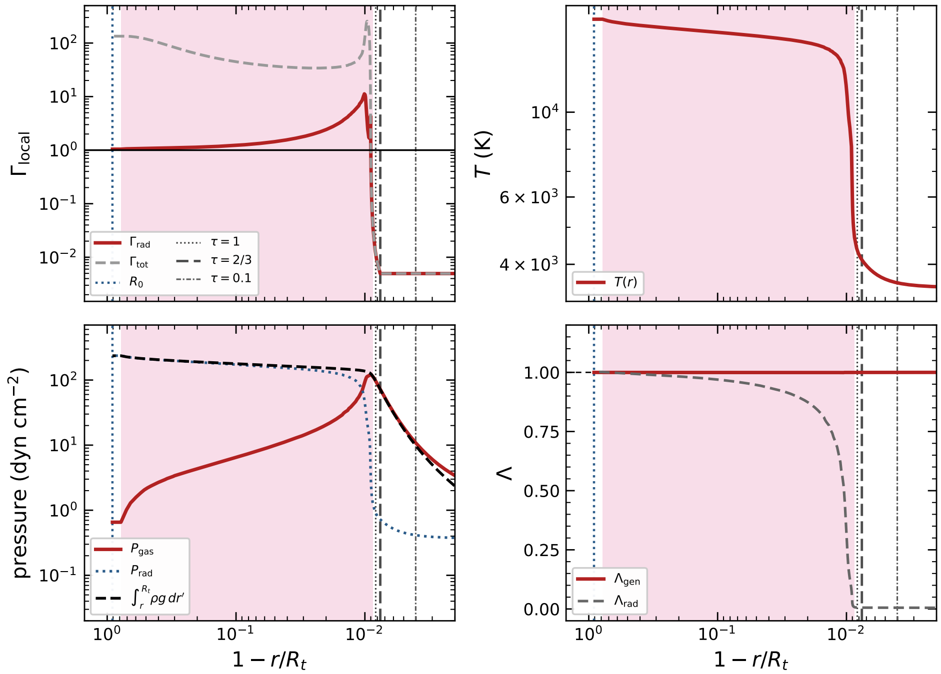

Figure A2. Radial structure of the converged $\alpha_{\rm acc} = 13.5$ model at $M_{\rm BH}/M_{\rm rad} = 0.10$ (where $M_{\rm rad}$ is the total mass interior to the radiative layer) and $T_{\rm eff} = 4109$ K. The models end at the top of the radiative layer and we attach the gray hydrostatic atmosphere analytically above it such that R_t is the top of that atmosphere's $\tau = 0.01$ surface. The pink band denotes the density inversions that occur when $\Gamma_{\rm rad} > 1$, and the vertical lines, identified in the top left legend, mark the inner boundary R_0 and the $\tau = 1$, $\tau = 2/3$, and $\tau = 0.1$ surfaces. *Top left:* the local Eddington ratios of Equation (6) for the radiative flux (solid) and the total flux (dashed). *Top right:* the temperature profile. *Bottom left:* the gas pressure, the radiation pressure $P_{\rm rad} = aT^4/3$, and the weight of the atmosphere above that layer. *Bottom right:* the launch number Λ of Equation (A2) (solid), which MESA's hydrostatic assumption forces to be unity, and the radiative share $\Lambda_{\rm rad}$ (dashed).

$P_{\rm rad} = aT^4/3$. By the conservation of momentum, the gas in a spherically symmetric envelope must obey

$$\rho \frac{Dv}{Dt} = -\frac{\partial}{\partial r}\left(P_{\rm gas} + P_B\right) - \frac{Gm\rho}{r^2} + \frac{\kappa\rho\, \ell_{\rm rad}}{4\pi r^2 c} + \rho\, \Omega^2 r, \tag{A1}$$

where v is the radial velocity, $P_{\rm gas} = \rho k_B T/(\mu m_p)$ is the gas pressure for temperature T, Boltzmann constant k_B, mean molecular weight μ, and proton mass m_p, $P_B = B^2/8\pi$ is the magnetic pressure for field strength B, Ω is the rotation rate, and the third term is the radiative force per unit volume, $\Gamma_{\rm rad}\, \rho g$.

We then integrate Equation (A1) from r to the top of the gray atmosphere (R_t) and define $W(r) = \int_r^{R_t} \rho g\, dr'$ as the total weight of the atmosphere above the layer r, giving the launch criterion $\Lambda(r)$ as

$$\Lambda(r) = \frac{1}{W(r)}\left[\int_r^{R_t} \Gamma_{\rm rad}\, \rho g\, dr' + \Delta P_{\rm gas} + \Delta P_B + \int_r^{R_t} \rho\, \Omega^2 r'\, dr'\right], \tag{A2}$$

where $\Delta P_{\rm gas} = P_{\rm gas}(r) - P_{\rm gas}(R_t)$ and ΔP_B is its magnetic counterpart. Launching a wind requires $\Lambda > 1$. Although written generally here, the magnetic and rotational terms are negligible and set to 0 throughout our calculations.

Since MESA is a hydrostatic code, $\Lambda(r)$ is trivially 1 throughout the entire envelope to within 3×10^{-4}. However, we can now separate out the radiative and gas shares. The radiative share, $\Lambda_{\rm rad}(r) \equiv W^{-1} \int_r^{R_t} \Gamma_{\rm rad}\, \rho g\, dr'$, is the fraction of the atmosphere's weight above r that the radiation alone supports. If the rotational and magnetic terms are negligible, then, in equilibrium, the launch condition is satisfied when $\Delta P_{\rm gas} = W\,(1 - \Lambda_{\rm rad})$.

B. HIGHER-ORDER CORRECTIONS TO THE MASS SCALE

This appendix describes further corrections that one could apply to the $\alpha_{\rm acc} = \phi\, f(Z)$ map, all of which can affect the black hole masses that we derive. In brief, we quantify how $g_{\rm dyn}$, magnetic support, a plane-parallel bias, and rotation affect our observed ϕ values, and we conclude that none of these phenomena changes our black hole mass bound by more than a factor of two.

B.1. *The Dynamical Term*

Our spectral fits assume $g_{\rm dyn} \approx 0$, where $g_{\rm dyn} \simeq -{\rm sgn}(dv^2/dR)v^2/R = g_{\rm net} - g$ is the bulk-motion term of Section 2.2 that describes any inwards or outwards motion of a layer at radius R and velocity v. Here, $g = \frac{GM_\star}{R_\star^2}$ is the physical Newtonian surface gravity of the photosphere with total mass $M_\star$ and radius $R_\star$, while $g_{\rm net}$ is the observed surface gravity. Qualitatively, quasi-stars are stable for 1–20 Myr (J. B. Hassan et al. 2026; A. D. Santarelli et al. 2026a) while the mass-loss rates that we derive in Table 2 are much smaller than $M_\star$, so we do not expect this term to be significant. More rigorously, for a quasi-star with a total mass $M_\star$ and an envelope mass $M_{\rm env} \equiv M_\star - M_{\rm BH} \geq 0.67\,M_\star$ that is losing mass at a rate $\dot{M}_{\rm wind}$, the bulk velocity of the photosphere can change by at most $v_{\rm esc}$ over the depletion timescale $t_{\rm dep} = M_{\rm env}/\dot{M}_{\rm wind}$. Using the fact that the dynamical free-fall timescale is $t_{\rm dyn} \approx (R_\star^3/GM_\star)^{1/2} \approx \frac{v_{\rm esc}}{\sqrt{2}g}$, we find that $g_{\rm dyn}$ can be at most

$$\frac{|g_{\rm dyn}|}{g} \leq \frac{v_{\rm esc}\,\dot{M}_{\rm wind}}{g\,M_{\rm env}} = \sqrt{2}\,\frac{t_{\rm dyn}}{t_{\rm dep}}. \tag{B3}$$

We evaluate Equation (B3) with the fitted masses and the mass-loss rates of Table 2, finding that, for The Egg, $|g_{\rm dyn}|/g \leq 2\times10^{-2}$, which implies dynamical times of 20–200 yr and depletion times of $\sim10^4$ yr. Since $M_\star \propto g$, we conclude that $g_{\rm dyn}$ can only shift our masses by at most a few percent. We conclude this section by warning that the actual dynamical situation of the photospheres may be more complex than this, but, as a matter of self-consistency, $g_{\rm dyn}/g \ll 1$ is a safe assumption.

B.2. *Non-Zero Angular Momentum*

Accretion supplies angular momentum at a rate of $f_j\, j_{\rm K}\dot{M}_{\rm acc}$, where f_j is the fraction of the Keplerian value that the arriving gas has, $j_{\rm K} = (GM_\star R_\star)^{1/2}$ is the Keplerian specific angular momentum at the surface, and $\dot{M}_{\rm acc}$ is the rate at which the envelope gains mass. We adopt $f_j \approx 0.01$ from the $\Omega\Gamma$ limit that L. Haemmerlé et al. (2018) derive, which they describe as the rotation rate at which rotation and radiation pressure counteract gravity. A magnetized wind removes angular momentum at $\frac{2}{3}\dot{M}_{\rm wind}\,\Omega R_{\rm A}^2$, where $\dot{M}_{\rm wind}$ is the mass-loss rate, Ω is the angular velocity, and $R_{\rm A}$ is the Alfvén radius (i.e., the distance out to which the field forces the wind to corotate; A. Ud-Doula et al. 2009). Conservation then dictates that

$$f_\Omega \equiv \frac{\Omega}{\Omega_{\rm crit}} = \frac{3}{2}\,f_j\,\frac{\dot{M}_{\rm acc}}{\dot{M}_{\rm wind}}\left(\frac{R_\star}{R_{\rm A}}\right)^2, \tag{B4}$$

where f_Ω is the angular velocity in units of the critical rate $\Omega_{\rm crit} = (GM_\star/R_\star^3)^{1/2}$.

We evaluate the Alfvén radius with $R_{\rm A}/R_\star \approx 0.29 + (\eta_* + 1/4)^{1/4}$, where the wind magnetic confinement parameter $\eta_* = B_{\rm eq}^2 R_\star^2/(\dot{M}_{\rm wind}v_\infty)$ is the field energy density divided by the wind kinetic energy density, $B_{\rm eq}$ is the equatorial surface field, and v_∞ is the terminal wind speed (A. Ud-Doula et al. 2008, 2009). η_* scales as $R_\star^2$, where $R_\star \sim 10^{16}$ cm, so η_* reaches 1.4 to 31 and $R_{\rm A}/R_\star$ is 1.4 to 2.7. In steady state, $f_j = 0.01$ gives $f_\Omega = 0.003$ to 0.009, and, even if we let f_j span plus or minus a decade, reaches only $f_\Omega \sim 10^{-4}$.

Rotation can cause the equatorial measurement of g to vary by von Zeipel's theorem, i.e., $g_{\rm eff} = g(1-f_\Omega^2)$ (H. von Zeipel 1924). The inferred Eddington ratio then becomes,

$$\Gamma_{\rm es} = \phi\left(1 - f_\Omega^2\right). \tag{B5}$$

Even in the most conservative cases, this correction can only be a few percent at most.

B.3. *Pressure Balance in a Steady State Atmosphere*

We now derive the equilibrium condition of the inflow–outflow interface of Figure 1, which we use to estimate how different phenomena affect our mapping between ϕ and $\alpha_{\rm acc}$ (Equation (5)). Energy conservation dictates that

$$L_{\rm obs} = L_{\rm BH} + L_{\rm in} - \Delta L_{\rm wind}, \tag{B6}$$

where $L_{\rm in} = GM_\star\dot{M}_{\rm in}/R_\star$ is the accretion luminosity of the infall and $\Delta L_{\rm wind} = \frac{1}{2}\dot{M}_{\rm wind}(v_\infty^2 + v_{\rm esc}^2)$ is the power that the wind extracts. Dividing the equation by $L_{\rm Edd}(\kappa_{\rm es}) = 4\pi GM_\star c/\kappa_{\rm es}$ turns each term into an Eddington ratio, and we write the corresponding infall and wind terms as $\phi_{\rm in} = \kappa_{\rm es}\dot{M}_{\rm in}/(4\pi R_\star c)$ and $\phi_{\rm out} = \kappa_{\rm es}\dot{M}_{\rm wind}(v_\infty^2 + v_{\rm esc}^2)/(8\pi GM_\star c)$. Bound bulk motion, rotation, magnetic support, and our `TLUSTY` plane-parallel bias cause us to overpredict the true Eddington ratio as $\Gamma_{\rm es} = \phi\,(1 - f_\Omega^2)(1 - f_B)(1 - g_{\rm dyn}/g)\,10^{-\Delta\log g}$, where f_Ω is the spin of Appendix B.2, $f_B = P_B/P_{\rm tot}$ is the magnetic support

Table B1. Black hole mass bounds ($M_{BH} \leq 0.33\, M_\star$, in $M_\odot$) under the corrections of Equation (B7).

Assumption	$\times M_\star$	Egg	UNCOVER	WIDE	RS
baseline	1.00	225	1,776	8,794	4,880
$g_{dyn}/g = 0.02$	1.02	230	1,812	8,970	4,977
$f_B = 0.05$	1.05	236	1,865	9,234	5,124
$\Delta \log g = 0.05$	1.12	252	1,990	9,849	5,465
$f_\Omega = 0.6$	1.56	351	2,771	13,718	7,612
all combined	1.88	423	3,340	16,532	9,174

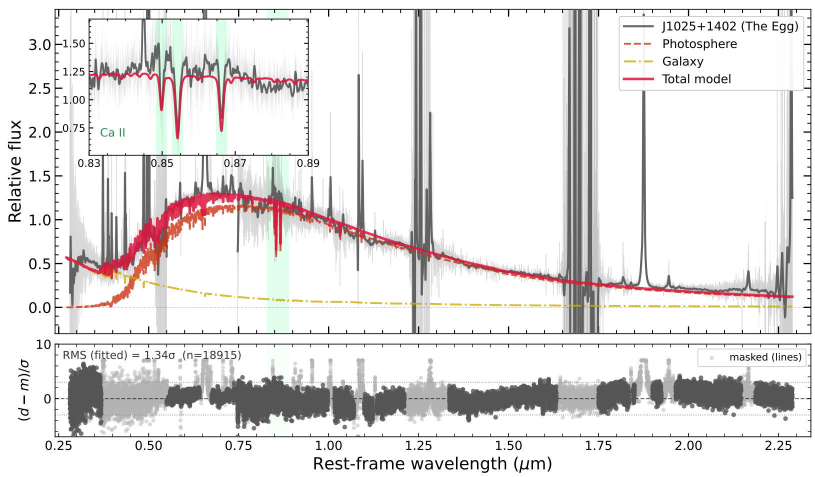

Figure C1. Fiducial fit to The Egg (J1025+1402, $z = 0.1007$). The dark gray curve is the combined MODS-B, MODS-R, and FIRE spectrum smoothed for display, with the unsmoothed data in light gray and the 1σ uncertainty band shaded. The red dashed curve is the TLUSTY photosphere ($T = 4502$ K), the gold dash-dotted curve is the host galaxy, and the crimson solid curve is the total model. The green vertical band marks the 0.83–0.89 μm Ca II triplet region, which the inset enlarges. The three narrow green bands inside the inset mark the individual Ca II lines.

fraction at the photosphere, $g_{dyn}/g \leq 2 \times 10^{-2}$ is the bound of Appendix B.1, and $\Delta \log g \geq 0$ is the plane-parallel bias in dex. Solving for α_{acc} then gives

$$\alpha_{acc} = f(Z)\left[\phi\left(1 - f_\Omega^2\right)(1 - f_B)\left(1 - g_{dyn}/g\right) 10^{-\Delta \log g} - \phi_{in} + \phi_{out}\right]. \tag{B7}$$

Table B1 uses this equation to summarize how each of these corrections affects our mass measurements.

C. ADDITIONAL SPECTRAL FITS

Figures C1, C2, and C3 show our fits to The Egg, UNCOVER-A2744-20698, and The Rosetta Stone as we describe in Section 4.

REFERENCES

Ackerman, A. S., & Marley, M. S. 2001, ApJ, 556, 872, doi: 10.1086/321540

Ashall, C., Naidu, R. P., Torralba, A., et al. 2026, arXiv e-prints, arXiv:2608.29011, doi: 10.48550/arXiv.2608.29011

Ball, W. H., Tout, C. A., & Żytkow, A. N. 2012, MNRAS, 421, 2713, doi: 10.1111/j.1365-2966.2012.20508.x

Ball, W. H., Tout, C. A., Żytkow, A. N., & Eldridge, J. J. 2011, MNRAS, 414, 2751, doi: 10.1111/j.1365-2966.2011.18591.x

Begelman, M. C. 2001, ApJ, 551, 897, doi: 10.1086/320240

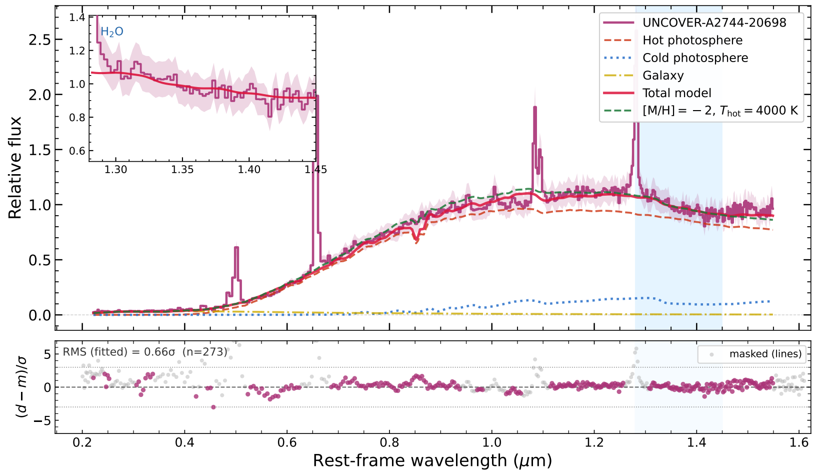

Figure C2. Fiducial two-component fit to UNCOVER-A2744-20698 (z = 2.42), whose hot photosphere fits at T = 3633 K and cold photosphere at T = 2338 K. The cold component again produces the water band, albeit ∼ 2 dex higher density than its hot component. As in Figure 3, the dark green curve shows the same model but with [M/H] = −2 and $T_{\rm hot}$ = 4000 K.

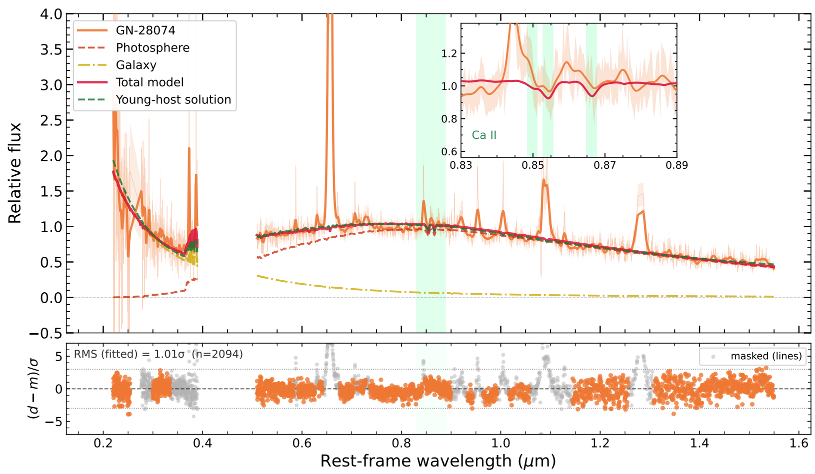

Figure C3. Fiducial fit to The Rosetta Stone (GN-28074, z = 2.26) across the G140M, G235M, and G395M gratings. The dark orange curve is the spectrum smoothed for display, the light orange line shows the unsmoothed data, and the gap near 0.4–0.5 μm separates the G140M and G235M wavelength gap. The red dashed curve is the TLUSTY photosphere (T = 4109 K), the gold dash-dotted curve is the host galaxy, and the crimson solid curve is the total model. The green vertical band marks the 0.83–0.89 μm Ca II triplet region, which the inset enlarges. The dark green curve shows a degenerate, low-ϕ, low M_* solution that fits the spectrum equally well (see Section 4.4).

Begelman, M. C. 2010, MNRAS, 402, 673, doi: 10.1111/j.1365-2966.2009.15916.x

Begelman, M. C., & Dexter, J. 2026, ApJ, 996, 48, doi: 10.3847/1538-4357/ae274a

Begelman, M. C., Rossi, E. M., & Armitage, P. J. 2008, MNRAS, 387, 1649, doi: 10.1111/j.1365-2966.2008.13344.x

Begelman, M. C., Volonteri, M., & Rees, M. J. 2006, MNRAS, 370, 289, doi: 10.1111/j.1365-2966.2006.10467.x

Bezanson, R., Labbe, I., Whitaker, K. E., et al. 2024, ApJ, 974, 92, doi: 10.3847/1538-4357/ad66cf

Bogdán, Á., Goulding, A. D., Natarajan, P., et al. 2024, Nature Astronomy, 8, 126, doi: 10.1038/s41550-023-02111-9

Bromm, V., & Loeb, A. 2003, ApJ, 596, 34, doi: 10.1086/377529

Campbell, C. B., Santarelli, A. D., & Caplan, M. E. 2025, Research Notes of the American Astronomical Society, 9, 185, doi: 10.3847/2515-5172/adef33

Cantiello, M., Hassan, J. B., Perna, R., et al. 2026, ApJL, 1000, L4, doi: 10.3847/2041-8213/ae4729

Carranza-Escudero, M., Conselice, C. J., Adams, N., et al. 2025, ApJL, 989, L50, doi: 10.3847/2041-8213/adf73d

Castor, J. I., Abbott, D. C., & Klein, R. I. 1975, ApJ, 195, 157, doi: 10.1086/153315

Cheng, S. J., Goldberg, J. A., Cantiello, M., et al. 2024, ApJ, 974, 270, doi: 10.3847/1538-4357/ad701e

Chisholm, J., Berg, D. A., Boylan-Kolchin, M., et al. 2026, ApJL, 1004, L4, doi: 10.3847/2041-8213/ae6dae

Chon, S., & Omukai, K. 2020, MNRAS, 494, 2851, doi: 10.1093/mnras/staa863

Conroy, C., Gunn, J. E., & White, M. 2009, ApJ, 699, 486, doi: 10.1088/0004-637X/699/1/486

Coughlin, E. R., & Begelman, M. C. 2024, ApJ, 970, 158, doi: 10.3847/1538-4357/ad5723

de Graaff, A., Hviding, R. E., Naidu, R. P., et al. 2025a, arXiv e-prints, arXiv:2511.21820, doi: 10.48550/arXiv.2511.21820

de Graaff, A., Brammer, G., Weibel, A., et al. 2025b, A&A, 697, A189, doi: 10.1051/0004-6361/202452186

DESI Collaboration, Abdul Karim, M., Adame, A. G., et al. 2026, AJ, 171, 285, doi: 10.3847/1538-3881/ae4c43

D'Eugenio, F., Maiolino, R., Perna, M., et al. 2026, MNRAS, 547, stag401, doi: 10.1093/mnras/stag401

Draine, B. T., & Li, A. 2007, ApJ, 657, 810, doi: 10.1086/511055

Eisenstein, D. J., Willott, C., Alberts, S., et al. 2026, ApJS, 283, 6, doi: 10.3847/1538-4365/ae3163

Fiacconi, D., & Rossi, E. M. 2016, MNRAS, 455, 2, doi: 10.1093/mnras/stv2237

Fu, S., Zhang, Z., Jiang, D., et al. 2026, Nature Astronomy, doi: 10.1038/s41550-026-02885-8

Fujii, M. S., Wang, L., Tanikawa, A., Hirai, Y., & Saitoh, T. R. 2024, Science, 384, 1488, doi: 10.1126/science.adi4211

Gentile, F., Giavalisco, M., Daddi, E., et al. 2026, arXiv e-prints, arXiv:2606.06575, doi: 10.48550/arXiv.2606.06575

González-Torà, G., Wittkowski, M., Davies, B., & Plez, B. 2024, A&A, 683, A19, doi: 10.1051/0004-6361/202348047

González-Torà, G., Wittkowski, M., Davies, B., Plez, B., & Kravchenko, K. 2023, A&A, 669, A76, doi: 10.1051/0004-6361/202244503

Gordon, K. D., Clayton, G. C., Misselt, K. A., Landolt, A. U., & Wolff, M. J. 2003, ApJ, 594, 279, doi: 10.1086/376774

Gräfener, G., Owocki, S. P., & Vink, J. S. 2012, A&A, 538, A40, doi: 10.1051/0004-6361/201117497

Greene, J. E., Labbe, I., Goulding, A. D., et al. 2024, ApJ, 964, 39, doi: 10.3847/1538-4357/ad1e5f

Greene, J. E., Setton, D. J., Furtak, L. J., et al. 2026, ApJ, 996, 129, doi: 10.3847/1538-4357/ae1836

Haemmerlé, L., Woods, T. E., Klessen, R. S., Heger, A., & Whalen, D. J. 2018, ApJL, 853, L3, doi: 10.3847/2041-8213/aaa462

Harikane, Y., Zhang, Y., Nakajima, K., et al. 2023, ApJ, 959, 39, doi: 10.3847/1538-4357/ad029e

Hassan, J. B., Perna, R., Cantiello, M., et al. 2026, ApJ, 998, 65, doi: 10.3847/1538-4357/ae3002

Heintz, K. E., Brammer, G. B., Watson, D., et al. 2025, A&A, 693, A60, doi: 10.1051/0004-6361/202450243

Hinshaw, G., Larson, D., Komatsu, E., et al. 2013, ApJS, 208, 19, doi: 10.1088/0067-0049/208/2/19

Höfner, S., & Olofsson, H. 2018, A&A Rv, 26, 1, doi: 10.1007/s00159-017-0106-5

Hubeny, I. 1988, Computer Physics Communications, 52, 103, doi: 10.1016/0010-4655(88)90177-4

Hubeny, I., Allende Prieto, C., Osorio, Y., & Lanz, T. 2021, arXiv e-prints, arXiv:2104.02829, doi: 10.48550/arXiv.2104.02829

Hviding, R. E., de Graaff, A., Miller, T. B., et al. 2025, A&A, 702, A57, doi: 10.1051/0004-6361/202555816

Hviding, R. E., de Graaff, A., Liu, H., et al. 2026, ApJL, 1000, L18, doi: 10.3847/2041-8213/ae4c88

Inayoshi, K., Visbal, E., & Haiman, Z. 2020, ARA&A, 58, 27, doi: 10.1146/annurev-astro-120419-014455

Jermyn, A. S., Bauer, E. B., Schwab, J., et al. 2023, ApJS, 265, 15, doi: 10.3847/1538-4365/acae8d

Ji, X., Maiolino, R., Übler, H., et al. 2025, MNRAS, 544, 3900, doi: 10.1093/mnras/staf1867

Ji, X., Pezzulli, G., D'Eugenio, F., et al. 2026, arXiv e-prints, arXiv:2604.03370, doi: 10.48550/arXiv.2604.03370

Jiang, Y.-F., Cantiello, M., Bildsten, L., Quataert, E., & Blaes, O. 2015, ApJ, 813, 74, doi: 10.1088/0004-637X/813/1/74

Johnson, B. D., Leja, J., Conroy, C., & Speagle, J. S. 2021, ApJS, 254, 22, doi: 10.3847/1538-4365/abef67

Juodžbalis, I., Ji, X., Maiolino, R., et al. 2024, MNRAS, 535, 853, doi: 10.1093/mnras/stae2367

Juodžbalis, I., Ji, X., D'Eugenio, F., et al. 2026, arXiv e-prints, arXiv:2607.19057, doi: 10.48550/arXiv.2607.19057

Kapoor, S., Matthee, J., Torralba, A., et al. 2026, arXiv e-prints, arXiv:2607.00084, doi: 10.48550/arXiv.2607.00084

Kido, D., Ioka, K., Hotokezaka, K., Inayoshi, K., & Irwin, C. M. 2025, MNRAS, 544, 3407, doi: 10.1093/mnras/staf1898

Kocevski, D. D., Onoue, M., Inayoshi, K., et al. 2023, ApJL, 954, L4, doi: 10.3847/2041-8213/ace5a0

Kocevski, D. D., Finkelstein, S. L., Barro, G., et al. 2025, ApJ, 986, 126, doi: 10.3847/1538-4357/adbc7d

Kokorev, V., Caputi, K. I., Greene, J. E., et al. 2024, ApJ, 968, 38, doi: 10.3847/1538-4357/ad4265

Kokorev, V., Chisholm, J., Naidu, R. P., et al. 2026, ApJ, 1004, 153, doi: 10.3847/1538-4357/ae4ed7

Kroupa, P. 2001, MNRAS, 322, 231, doi: 10.1046/j.1365-8711.2001.04022.x

Labbe, I., Greene, J. E., Bezanson, R., et al. 2025, ApJ, 978, 92, doi: 10.3847/1538-4357/ad3551

Lambrides, E., Larson, R. L., Garofali, K., et al. 2026, Nature Astronomy, 10, 868, doi: 10.1038/s41550-026-02813-w

Lamers, H. J. G. L. M., & Cassinelli, J. P. 1999, Introduction to Stellar Winds

Lebzelter, T., Heiter, U., Abia, C., et al. 2012, A&A, 547, A108, doi: 10.1051/0004-6361/201219142

Lin, X., Fan, X., Cai, Z., et al. 2026a, ApJ, 997, 364, doi: 10.3847/1538-4357/ae2bdf

Lin, X., Fan, X., Cai, Z., et al. 2026b, arXiv e-prints, arXiv:2605.21574, doi: 10.48550/arXiv.2605.21574

Lin, X., Fan, X., Sun, F., et al. 2026c, ApJ, 997, 61, doi: 10.3847/1538-4357/ae1eef
Liu, H., Jiang, Y.-F., Quataert, E., Greene, J. E., & Ma, Y. 2025, ApJ, 994, 113, doi: 10.3847/1538-4357/ae0c19
Liu, H., Jiang, Y.-F., Quataert, E., et al. 2026, arXiv e-prints, arXiv:2603.02317, doi: 10.48550/arXiv.2603.02317
Liu, J.-R., Feng, H., & Ho, L. C. 2026, arXiv e-prints, arXiv:2607.17448, doi: 10.48550/arXiv.2607.17448
Loiacono, F., Gilli, R., Mignoli, M., et al. 2026, arXiv e-prints, arXiv:2606.30253, doi: 10.48550/arXiv.2606.30253
Luo, Y., Shlosman, I., Nagamine, K., & Fang, T. 2020, MNRAS, 492, 4917, doi: 10.1093/mnras/staa153
Madau, P., & Maiolino, R. 2026, arXiv e-prints, arXiv:2602.22386, doi: 10.48550/arXiv.2602.22386
Madau, P., & Rees, M. J. 2001, ApJL, 551, L27, doi: 10.1086/319848
Maiolino, R., Scholtz, J., Witstok, J., et al. 2024, Nature, 627, 59, doi: 10.1038/s41586-024-07052-5
Marigo, P., & Aringer, B. 2009, A&A, 508, 1539, doi: 10.1051/0004-6361/200912598
Maseda, M. V., de Graaff, A., Franx, M., et al. 2024, A&A, 689, A73, doi: 10.1051/0004-6361/202449914
Matthee, J., Naidu, R. P., Brammer, G., et al. 2024, ApJ, 963, 129, doi: 10.3847/1538-4357/ad2345
Matthee, J., Torralba, A., Pezzulli, G., et al. 2026, arXiv e-prints, arXiv:2603.17667, doi: 10.48550/arXiv.2603.17667
Miles, B. E., Biller, B. A., Patapis, P., et al. 2023, ApJL, 946, L6, doi: 10.3847/2041-8213/acb04a
Naidu, R. P., Matthee, J., Katz, H., et al. 2026a, Nature, 656, 329, doi: 10.1038/s41586-026-10846-4
Naidu, R. P., Matthee, J., de Graaff, A., et al. 2026b, arXiv e-prints, arXiv:2606.30711, doi: 10.48550/arXiv.2606.30711
Nandal, D., Chilingarian, I. V., Nagele, C., et al. 2026, ApJL, 1006, L21, doi: 10.3847/2041-8213/ae82f3
Owocki, S. P., Gayley, K. G., & Shaviv, N. J. 2004, ApJ, 616, 525, doi: 10.1086/424910
Pacucci, F., Hernquist, L., & Fujii, M. 2025, ApJ, 994, 40, doi: 10.3847/1538-4357/ae1619
Pacucci, F., & Narayan, R. 2024, ApJ, 976, 96, doi: 10.3847/1538-4357/ad84f7
Pacucci, F., Nguyen, B., Carniani, S., Maiolino, R., & Fan, X. 2023, ApJL, 957, L3, doi: 10.3847/2041-8213/ad0158
Pan, Z., Zhuang, M.-Y., Shen, Y., et al. 2026, arXiv e-prints, arXiv:2606.09721, doi: 10.48550/arXiv.2606.09721
Park, K., Torralba, A., Matthee, J., et al. 2026, arXiv e-prints, arXiv:2605.14233, doi: 10.48550/arXiv.2605.14233
Paxton, B., Bildsten, L., Dotter, A., et al. 2011, ApJS, 192, 3, doi: 10.1088/0067-0049/192/1/3
Paxton, B., Cantiello, M., Arras, P., et al. 2013, ApJS, 208, 4, doi: 10.1088/0067-0049/208/1/4
Paxton, B., Marchant, P., Schwab, J., et al. 2015, ApJS, 220, 15, doi: 10.1088/0067-0049/220/1/15
Paxton, B., Schwab, J., Bauer, E. B., et al. 2018, ApJS, 234, 34, doi: 10.3847/1538-4365/aaa5a8
Paxton, B., Smolec, R., Schwab, J., et al. 2019, ApJS, 243, 10, doi: 10.3847/1538-4365/ab2241
Pezzulli, E., Valiante, R., & Schneider, R. 2016, MNRAS, 458, 3047, doi: 10.1093/mnras/stw505
Portegies Zwart, S. F., & McMillan, S. L. W. 2002, ApJ, 576, 899, doi: 10.1086/341798
Quataert, E., Fernández, R., Kasen, D., Klion, H., & Paxton, B. 2016, MNRAS, 458, 1214, doi: 10.1093/mnras/stw365
Quataert, E., & Gruzinov, A. 2000, ApJ, 539, 809, doi: 10.1086/309267
Rantala, A. 2026, arXiv e-prints, arXiv:2604.22924, doi: 10.48550/arXiv.2604.22924
Rees, M. J. 1987, MNRAS, 228, 47P, doi: 10.1093/mnras/228.1.47P
Regan, J., & Volonteri, M. 2024, The Open Journal of Astrophysics, 7, 72, doi: 10.33232/001c.123239
Regan, J. A., Johansson, P. H., & Wise, J. H. 2016, MNRAS, 459, 3377, doi: 10.1093/mnras/stw899
Reines, A. E., & Volonteri, M. 2015, ApJ, 813, 82, doi: 10.1088/0004-637X/813/2/82
Roman-Garza, J., Charbonnel, C., Schaerer, D., et al. 2026, arXiv e-prints, arXiv:2603.21714, doi: 10.48550/arXiv.2603.21714
Rusakov, V., Watson, D., Nikopoulos, G. P., et al. 2026, Nature, 649, 574, doi: 10.1038/s41586-025-09900-4
Santarelli, A. D., Campbell, C. B., Farag, E., et al. 2026a, ApJ, 998, 150, doi: 10.3847/1538-4357/ae371e
Santarelli, A. D., Farag, E., Bellinger, E. P., et al. 2026b, ApJL, 998, L4, doi: 10.3847/2041-8213/ae3713
Shaviv, N. J. 2001, MNRAS, 326, 126, doi: 10.1046/j.1365-8711.2001.04574.x
Sok, V., Nelson, E. J., Begelman, M. C., et al. 2026, arXiv e-prints, arXiv:2606.23778, doi: 10.48550/arXiv.2606.23778
Speagle, J. S. 2020, MNRAS, 493, 3132, doi: 10.1093/mnras/staa278
Stern, J., & Laor, A. 2012, MNRAS, 423, 600, doi: 10.1111/j.1365-2966.2012.20901.x
Stone, Z., Shen, Y., Zhuang, M.-Y., et al. 2026, arXiv e-prints, arXiv:2608.01647, doi: 10.48550/arXiv.2608.01647
Sun, W. Q., Naidu, R. P., Matthee, J., et al. 2026, The Open Journal of Astrophysics, 9, 62505, doi: 10.33232/001c.162505
Takasao, S., & Inayoshi, K. 2026, arXiv e-prints, arXiv:2605.21589, doi: 10.48550/arXiv.2605.21589
Tang, M., Stark, D. P., Mason, C. A., et al. 2026, arXiv e-prints, arXiv:2604.03563, doi: 10.48550/arXiv.2604.03563
Taylor, A. J., Kokorev, V., Kocevski, D. D., et al. 2025, ApJL, 989, L7, doi: 10.3847/2041-8213/ade789

Ud-Doula, A., Owocki, S. P., & Townsend, R. H. D. 2008, MNRAS, 385, 97, doi: 10.1111/j.1365-2966.2008.12840.x

Ud-Doula, A., Owocki, S. P., & Townsend, R. H. D. 2009, MNRAS, 392, 1022, doi: 10.1111/j.1365-2966.2008.14134.x

Umeda, H., Inayoshi, K., Harikane, Y., & Murase, K. 2026, ApJ, 999, 183, doi: 10.3847/1538-4357/ae4101

van Marle, A. J., Owocki, S. P., & Shaviv, N. J. 2008, MNRAS, 389, 1353, doi: 10.1111/j.1365-2966.2008.13648.x

von Zeipel, H. 1924, MNRAS, 84, 665, doi: 10.1093/mnras/84.9.665

Wakeford, H. R., Visscher, C., Lewis, N. K., et al. 2017, MNRAS, 464, 4247, doi: 10.1093/mnras/stw2639

Walker, M. F. 1972, ApJ, 175, 89, doi: 10.1086/151540

Wang, B., de Graaff, A., Davies, R. L., et al. 2025, ApJ, 984, 121, doi: 10.3847/1538-4357/adc1ca

Wang, B., Leja, J., Labbe, I., et al. 2026, arXiv e-prints, arXiv:2602.06024, doi: 10.48550/arXiv.2602.06024

Weibel, A., Naidu, R. P., Oesch, P. A., et al. 2026, arXiv e-prints, arXiv:2606.17271, doi: 10.48550/arXiv.2606.17271

Yanagisawa, H., Ouchi, M., Kiyota, T., et al. 2026, arXiv e-prints, arXiv:2607.26269, doi: 10.48550/arXiv.2607.26269

York, D. G., Adelman, J., Anderson, Jr., J. E., et al. 2000, AJ, 120, 1579, doi: 10.1086/301513

Zhang, Z., Li, M., Oguri, M., et al. 2025, arXiv e-prints, arXiv:2512.05180, doi: 10.48550/arXiv.2512.05180